Investigation of Corium Melt Interaction with NPP Reactor Vessel Steel (METCOR-P)

Intermediate report
01 / 01 / 11 – 31 / 03 / 11

INTERACTION OF MOLTEN CORIUM WITH VESSEL STEEL IN THE NEUTRAL ABOVE-MELT ATMOSPHERE AND VERTICAL POSITION OF THE INTERACTION INTERFACE

EXPERIMENT MCP-8

Project title	Investigation of Corium Melt Interaction with NPP Reactor Vessel Steel (METCOR-P #3592)	
Customer	ISTC	
File specification	RMP-08	
Location of project implementation	FGUP A.P. Alexandrov Research Institute of Technology (NITI) of The State Atomic Energy Corporation ROSATOM Russia, 188540, Sosnovy Bor Leningrad Region	
Project manager	Name	V.B. Khabensky
	Signature	
	Date	31.03.2011

Authors

Dr., Prof.	V.B. Khabensky
Dr., Prof	S.V. Bechta
Dr.	V.S. Granovsky
Dr.	S.A. Vitol
Dr.	S.Ju. Kotova
Dr., As. Prof	A.A. Sulatsky
Dr., As. Mem, RAS	V.V. Gusarov
Dr., As. Prof	D.B. Lopukh
	V.I. Almyashev
	E.V. Krushinov
	V.G. Blizniuk
	V.R. Bulighin
	E. K. Kalyago
	N.E. Kamensky
	A.V. Lysenko
	A.P. Martynov
	V.V. Martynov
	E.V. Shevchenko
	A.A. Chertkov
Dr.	S.A. Smirnov

CONTENTS

Introduction

In the ISTC METCOR and METCOR-P projects the vessel steel – molten corium interaction in the inert atmosphere was focused on the horizontal positioning of the interaction interface. In all experiments the melt composition included UO_2, ZrO_2 and Zr, and only in one (MC9) iron was present the melt, but by the end of experiment all of it and the corroded iron from the specimen evaporated [1]. In MCP-1 the interaction interface had a vertical orientation. The experiment determined the final corrosion depth and all interaction parameters except corrosion kinetics [2]. The latter was explained by the problem of corrosion depth measurements by ultrasonic sounding for the vertically-positioned specimen, which had not been resolved by that time.

In accordance with the METCOR-P Project Plan the MCP-8 has studied the interaction between vessel steel and the melt of stainless steel enriched with U and Zr. Its experimental objective was to determine the qualitative and quantitative interaction characteristics including the vessel steel corrosion kinetics.

The report presents the description and results of Pr-MCP8 pretest and MCP-8 test within the ISTC METCOR-P project carried out on the Rasplav-3 test facility in NITI, Sosnovy Bor.

MCP-8 has studied the vessel steel – corium melt interaction in the inert atmosphere (argon). The corium charge had the following composition, mass%: 39U + 14Zr + 48SS; the interaction interface had a vertical orientation and maximum temperature on the surface was ~1400ºC.

1. EXPERIMENT Pr- MCP8

1.1. Experiment preparation

Additional studies were necessary for efficient ultrasonic (US) measurements of corrosion.

Two alternative designs of the specimen are presented in figures 1.1–1.3.

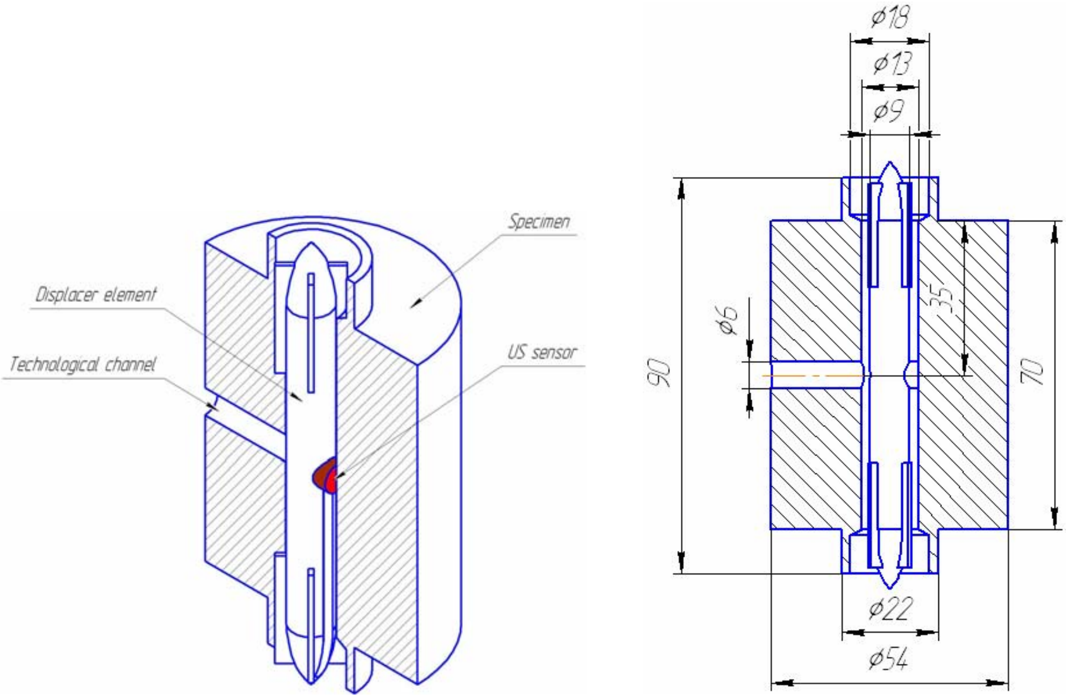

Fig. 1.1 – Steel specimen design (option 1)

1 –centering and reinforcement ribs 2 – location of the US sensor; 3 – technological channel; 4 – specimen; 6 – displacer, 7 – technological channel plug.

Fig. 1.2 – Steel specimen (option 1)

The specimen manufactured in accordance with design option 1 had a technological channel 3 for fitting the US sensor edge on the specimen wall. The miniature sensor was spring-loaded into displacer 6 (US sensor location – 2). The displacer with US sensor was installed into the central cooling channel and centered by ribs 1. The technological channel was closed by plug 7, and connections for cooling water in and out were welded.

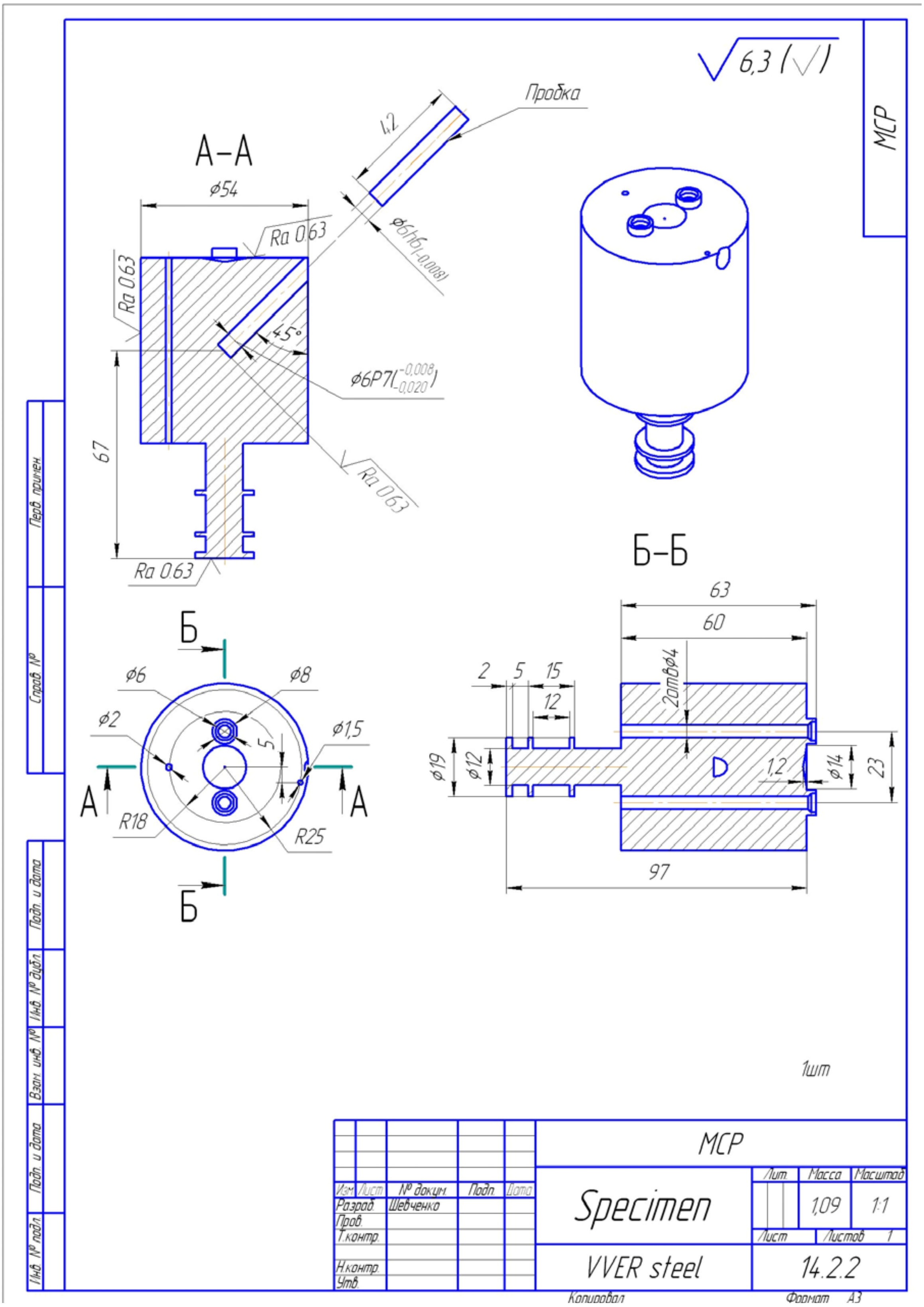

Fig. 1.3- Steel specimen design (option 2)

In comparison with MCP-1 the MCP-8 specimen diameter was substantially increased. Because of this a new IMCC furnace was designed and manufactured. It had the internal diameter of 100 mm. The HF generator capacity was increased for higher power output.

A miniature sensor was manufactured for design option 1. Its characteristics are given in Table 1.1.

Table 1.1 – US sensor characteristics

Range of measured thickness	Operation frequency	Bandwidth at the 6 DB level	Dimensions	Work surface temperature
15±7mm	5±0.2MHz	≥50%	Ø 6 mm, h=8±1mm	≤ 200ºC

Trial tests of the sensor were preformed on the 12.5 mm-thick plate in air. The results are given in Fig. 1.4

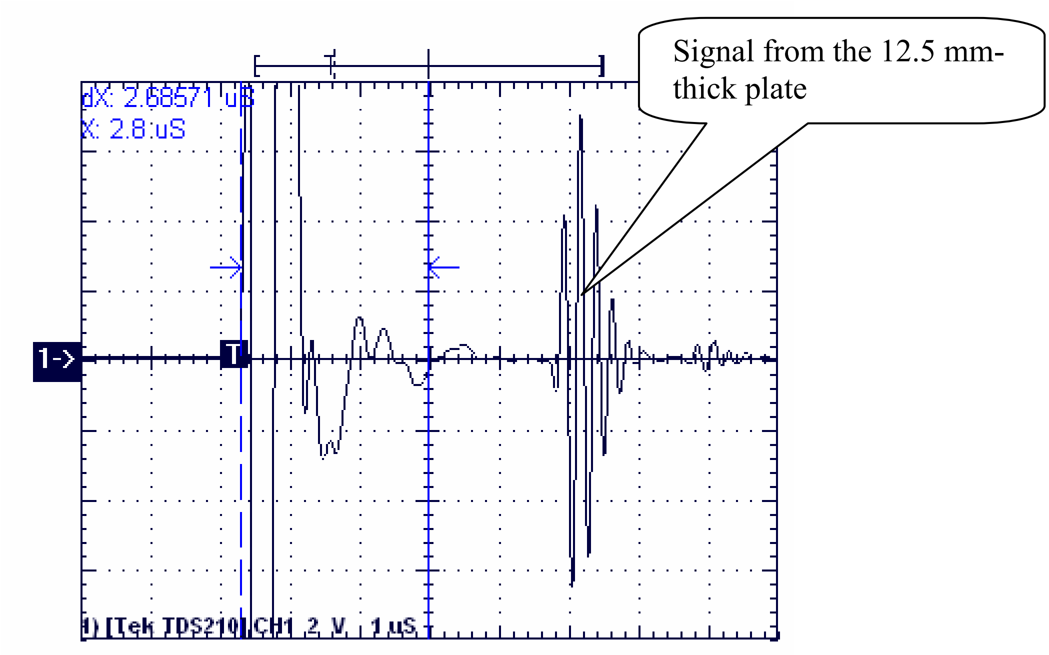

Fig. 1.4 – Oscillogram of echo-signal from the 12.5 mm-thick plate

During the trial test the reflected pulse sufficient for the amplitude recording was registered. As, in accordance with the experiment, the sensor is placed into the flow of cooling liquid, it was subjected to a trial on the same plate submerged in water. Fig 1.5 gives the test results.

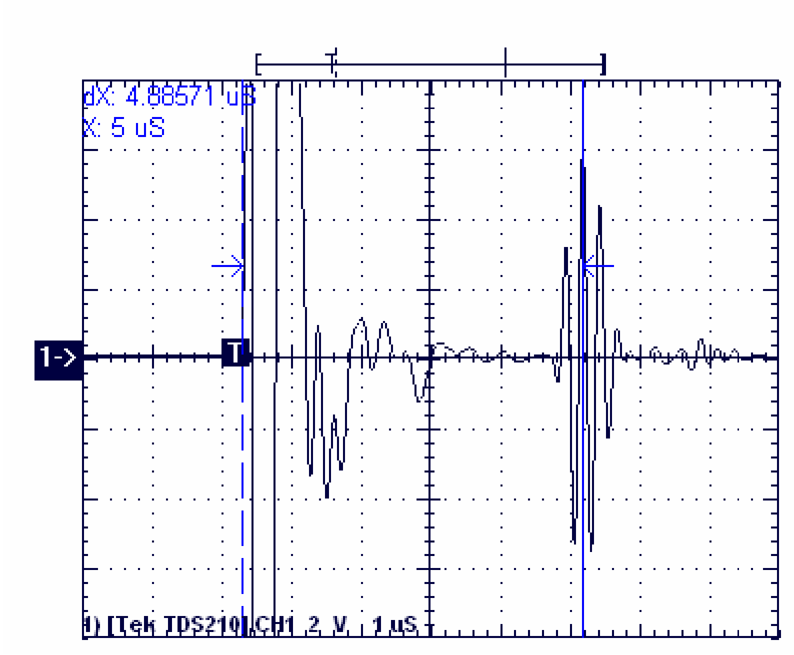

Fig. 1.5 - Oscillogram of echo-signal from the 12.5 mm-thick plate submerged in water

The presence of water did not produce any changes in the oscillogram, which confirmed the sensor efficiency in the experimental conditions. But echo signal from the specimen surface disappeared after the experimental section was assembled for tests with the specimen heating inside the inductor. The specimen and embedded sensor were inspected and it was found that the fastening of emitting crystal could not sustain the compressive load, which is even higher in the experimental conditions because of high-temperature deformations. For this reason the conclusion was made that the first design option was not applicable.

The 2nd specimen design option, due to its non-axisymmetricity, needed both the check of the US measurement of ablation and the cooling efficiency. The last-mentioned required a preliminary numerical modeling of the specimen temperature conditions. Its objective was to determine the heat flux on the surface of cooling channels at such heat flux on the specimen surface, which provides its maximum temperature of 1400ºC.

Calculations were made in the 2D formulation using the ANSYS code. Temperature field in the specimen is shown in Fig. 1.6. The maximum temperature (1400°C) is reached on the specimen surface on the symmetry plane between the cooling channels, i.e. in the plane of acoustic mirror (the plane of US measurements) at a 0.97 MW/m^2 on the specimen surface. At this the maximum heat flux to the surface of cooling channels was 7.4 MW/m^2. The evaluated critical heat flux to the modeled parameters of the cooling water is 12 MW/m^2 and, consequently, DNB margin ~1.6.

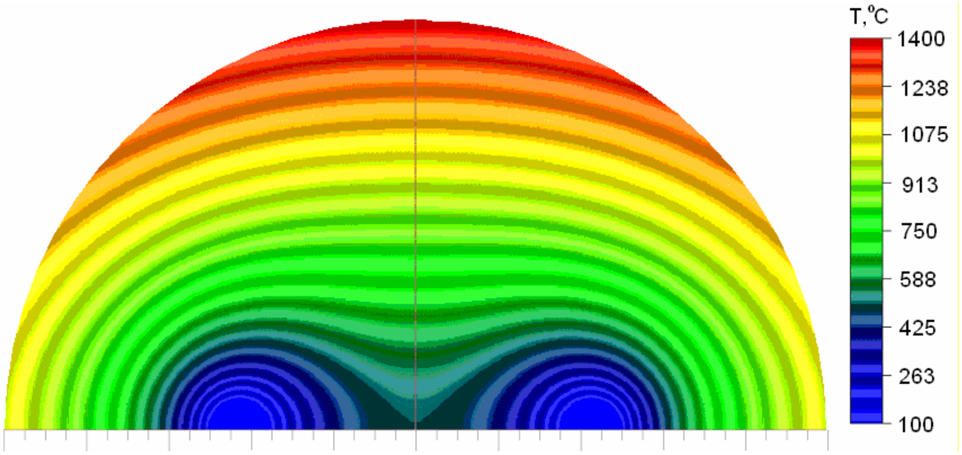

Fig. 1.6 – Temperature field in the specimen

After the numerical modeling a Pr-MCP8 pretest was made. Its task was to make an experimental check of the specimen cooling system operability and US measurements validity. As the pretest was made without the specimen-melt interaction, the change (reduction) of the specimen diameter was provided by its surface melting. Beside the check of the US measurement efficiency such method enabled to test the efficiency of the specimen cooling system in the most conservative conditions.

1.2. Pr-MCP8 specifications

Specimen in the inductor is shown in Fig. 1.7. The specimen (Fig. 1.3) had an acoustic defect of a 2 mm diameter on the 18 mm radius and a through borehole of 1.5 mm diameter on the 25 mm radius. To measure temperature on the specimen surface the acoustic defect and the borehole had two installed thermocouples T1, T2, K- type with hot junctions located at a 30 mm height. Each cooling channel had online calorimetric measurement in order to evaluate the total power deposited into the specimen.

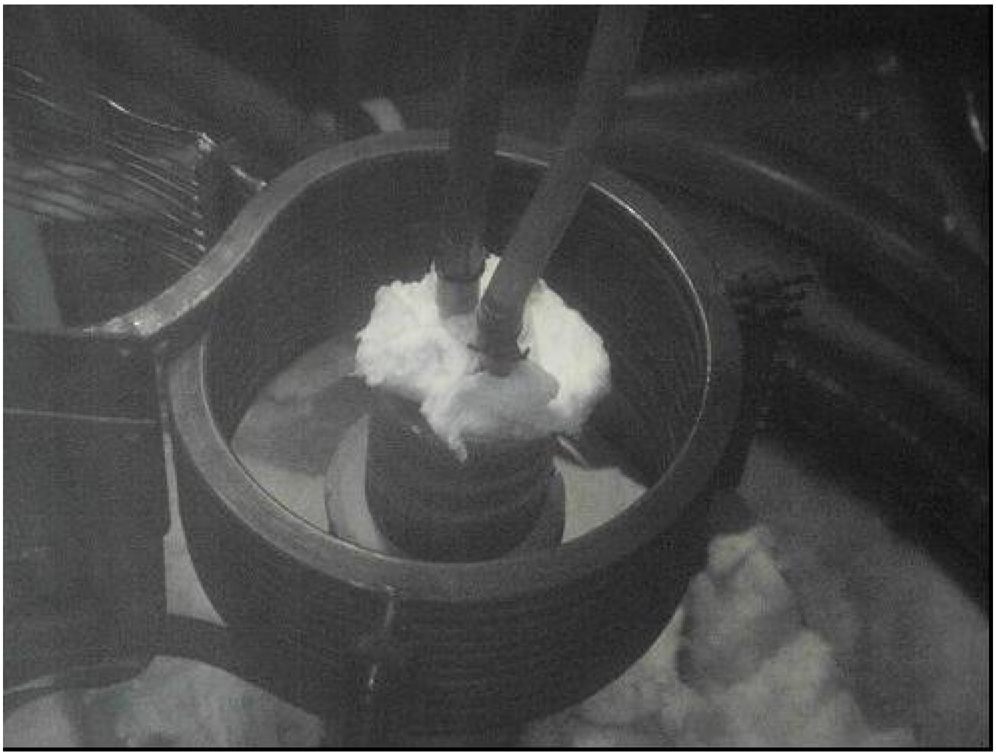

Fig. 1.7 – Specimen in the inductor

1.3. Experimental procedure

After the HF heating was turned on, the inductor voltage was stepped up and specimen surface temperature was monitored using the T1, T2 thermocouple readings. After the last voltage increase a sharp increase of thermocouple indications was registered, and specimen side surface melting was observed. When the molten metal started to pour down the side surface of the specimen, the HF heating was disconnected and the experiment was stopped. Fig. 1.8 gives the electric characteristics of the HF generator, dynamics of heat and electromagnetic fluxes into the specimen and thermocouple readings. A sharp temperature growth at the last stage of the experiment corresponds to the specimen ablation start. The experimental data on specimen ablation are given in Section 1.4.

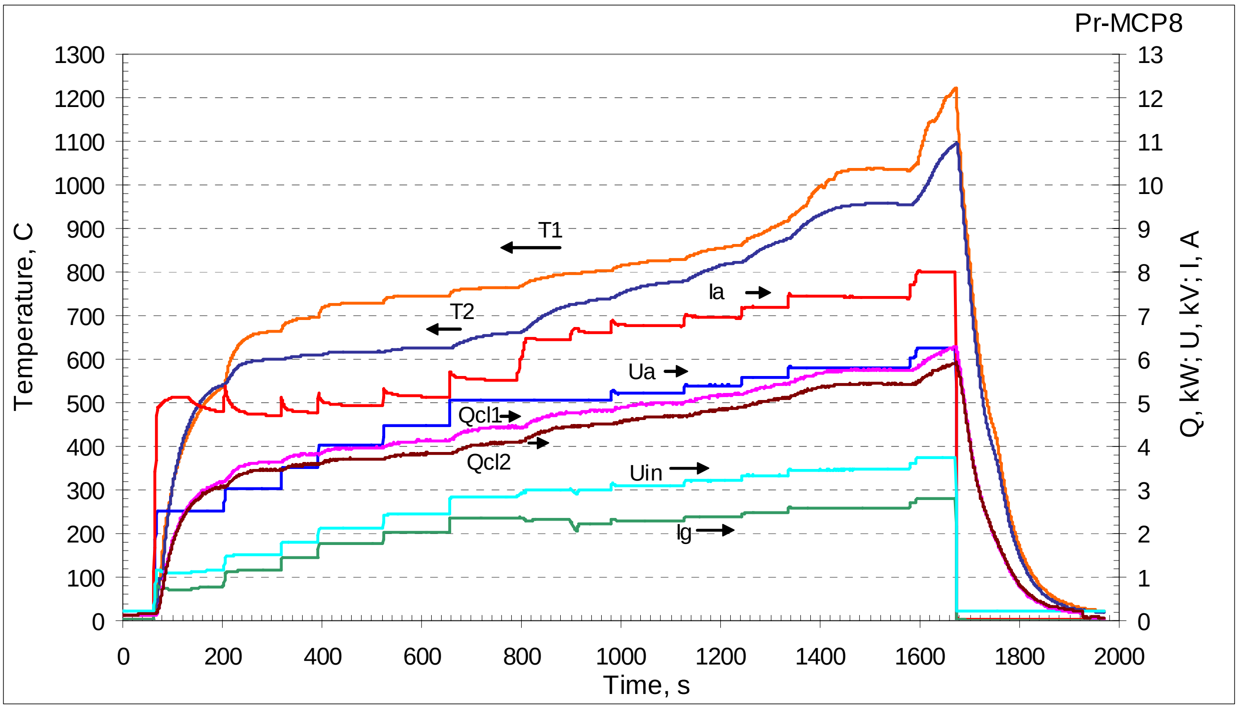

Fig. 1.8 – Plate current and voltage, inductor voltage, oscillating tube grid current, electromagnetic and heat fluxes in the cooling channels Qcl1 and Qcl2, thermocouple T1 (25 mm radius) and T2 (18 mm radius) versus time.

1.4. Posttest analysis

Photographs of Fig. 1.9 show two views of the specimen surface: across the acoustic mirror (left) and from the side perpendicular to the diameter plane of the acoustic mirror (right). In the ablation region covered by the US measurement an accretion of frozen melt is observed. Fig. 1.10 shows the top view of the specimen, there the locations of specimen surface ablation are quite distinct. For the direct measurement of specimen ablation depth its axial section was cut and a polished section shown in Fig. 1.11 was prepared (a metallic accretion on the specimen top was removed). Lines in the figure show the pathway: US sensor – acoustic mirror – specimen surface. In accordance with measurements the distance between the axis of acoustic mirror and the specimen surface decreased by 1 mm.

Fig. 1.9 – Specimen side surface (the USS monitoring area is marked by an oval)

Fig. 1.10 – Top view of the specimen (the USS monitoring area is marked by an oval)

Fig. 1.11 – Polished section in the of US measurement plane

Fig. 1.12 shows the online data of measured specimen ablation. The figure indicates the ablation start, period of melt spreading from the specimen top and the moment of inductor disconnection.

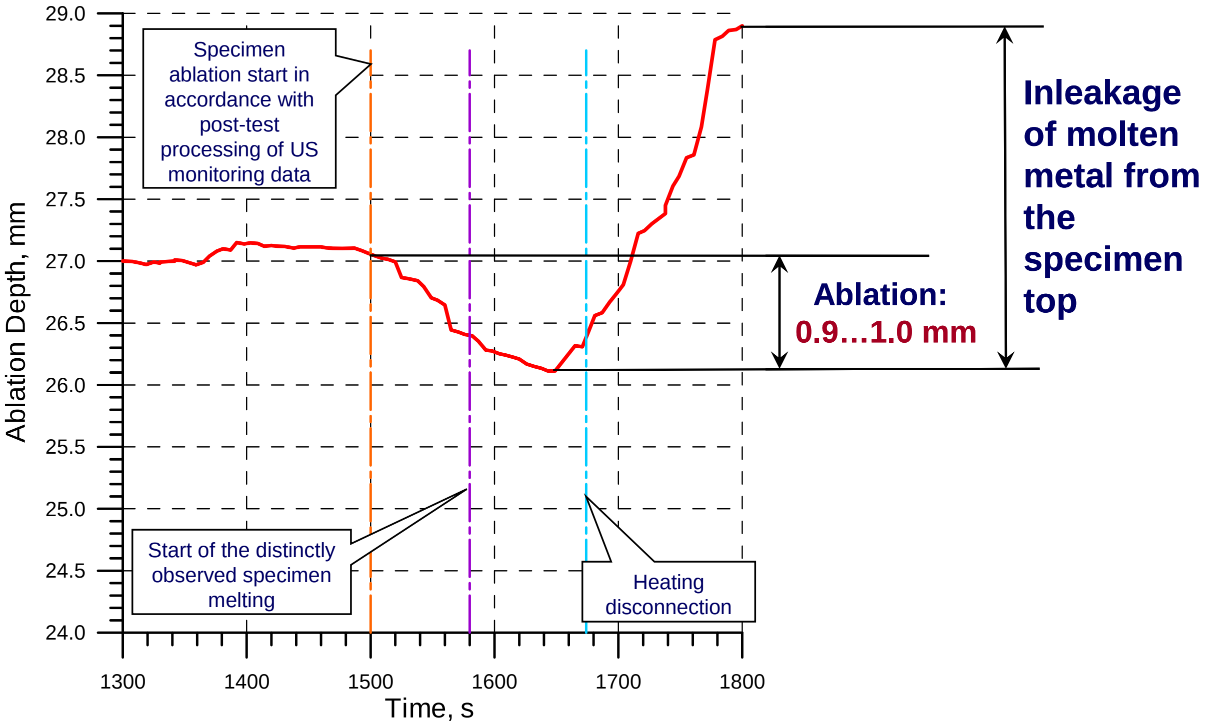

Fig. 1.12 – Specimen ablation dynamics during the pretest

1.5. Discussion of results.

First of all let us consider the US measurements of specimen ablation. It can be seen from Fig. 1.12 that the online measurements give an adequate picture of the specimen ablation and the increase of distance from the acoustic mirror to the freezing surface of the accretion. At this, the value of maximum ablation depth coincides with the posttest measurements, which is ≈1 mm. Therefore, the specimen design used in the pretest and the method of US measurements enable efficient monitoring of the specimen ablation during its interaction with melt.

The completed pretest also enabled to evaluate the heat flux to the specimen, at which its effective cooling is guaranteed. Fig. 1.13 shows heat flux from the specimen, and Fig. 1.14 – thermocouple measurements. The maximum registered power was ≈12 kW, which is higher than a value calculated for the MCP-8 conditions, and it can be used as a reference value for the test.

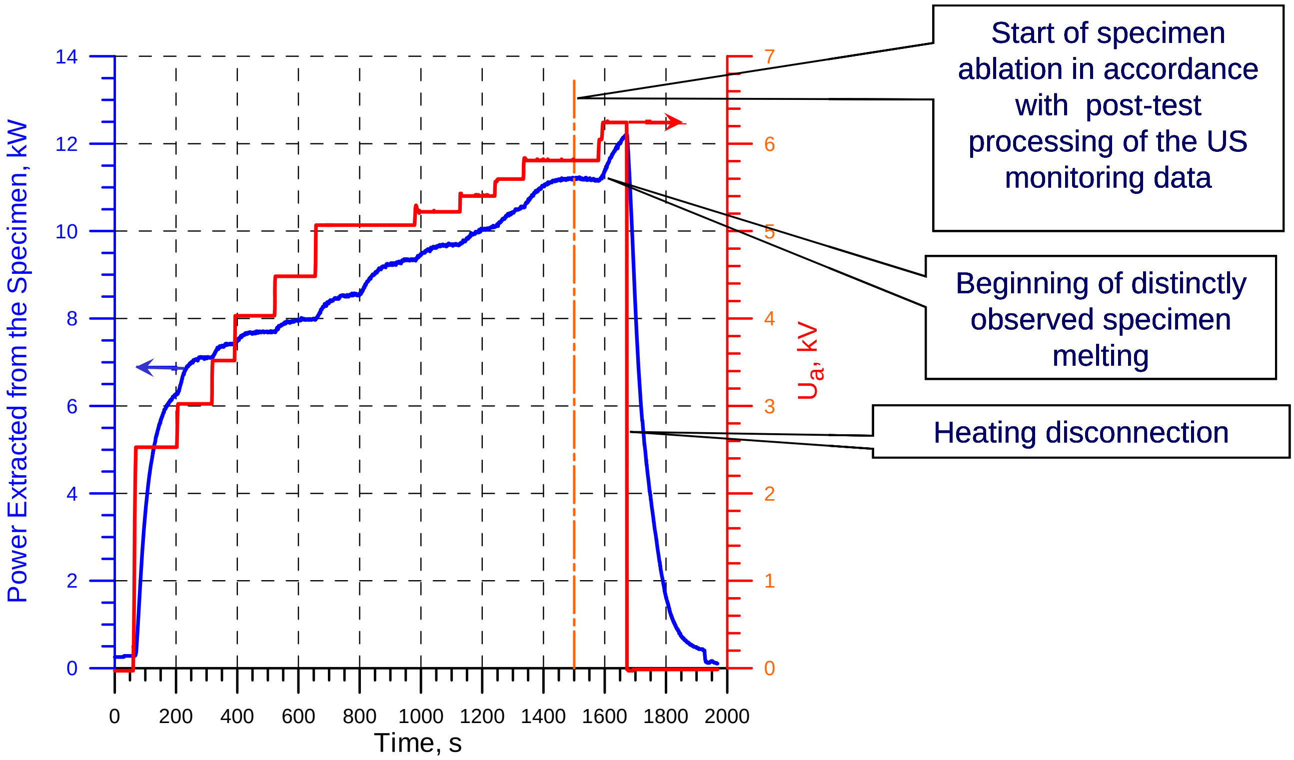

Fig. 1.13 – Heat transfer from the specimen and the inductor voltage versus time

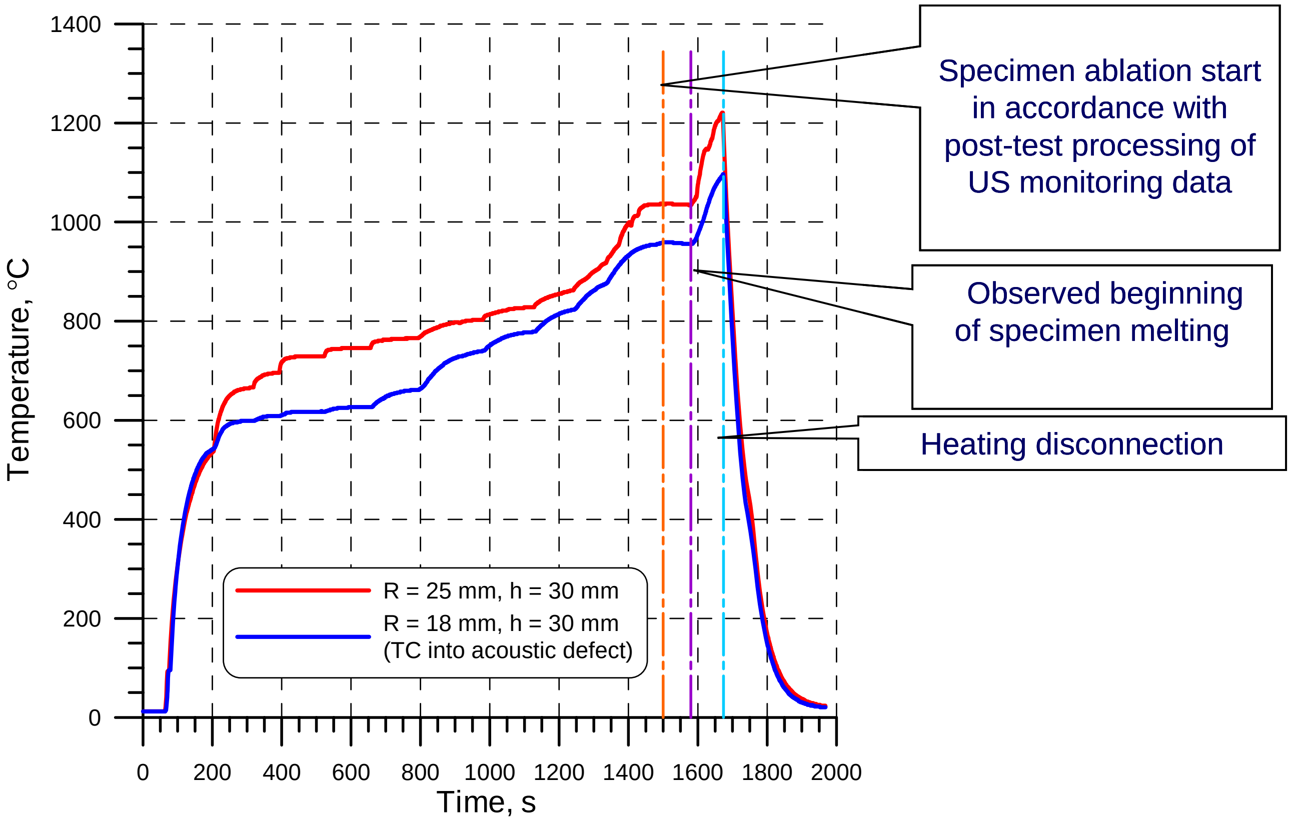

Fig. 1.14. Thermocouple readings

2. EXPERIMENT MCP-8

2.1. Experimental section schematics

As mentioned above, a new furnace was designed and manufactured for the experiment, and the HF generator was modified. The MCP-8 furnace schematics is shown in Fig. 2.1. Vessel steel specimen (4) is a 54 mm-diameter 60 mm-high cylinder with two cooling channels having 4 mm in diameter. The cylindrical specimen is mounted along the crucible section; it is rested on bottom calorimeter (6). Water-cooled shaft-screen (3) is placed above the specimen to screen the top connection of cooling water pipe. Two access ports covered by the quartz windows are made in the furnace cover to monitor the melt surface. Thermocouple location schematics is presented in Fig. 2.2 and Table 2.1. 1.5 mm-diameter boreholes were made in the specimen to accommodate K-type thermocouples.

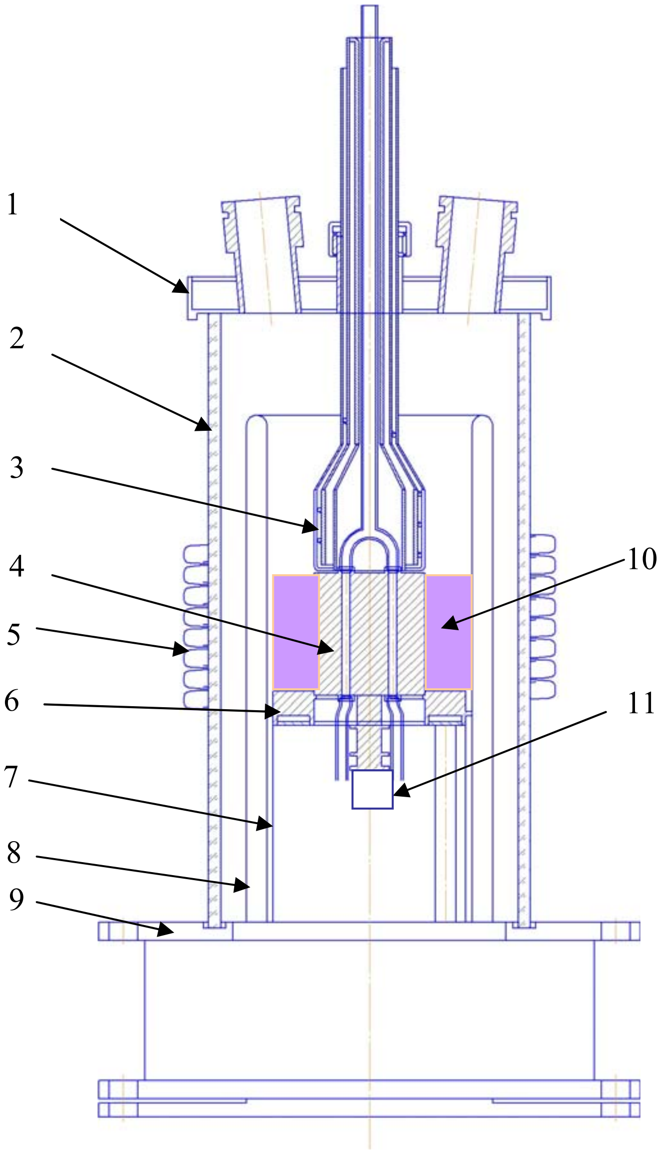

1 – water-cooled cover, 2 – quartz tube, 3 – water-cooled screen-shaft, 4 – vessel steel specimen, 5 – inductor, 6 – bottom calorimeter, 7 – calorimeter support, 8 –crucible section, 9 – water-cooled screen, 10 – molten pool, 11 - US sensor

Fig. 2.1 – Furnace schematics

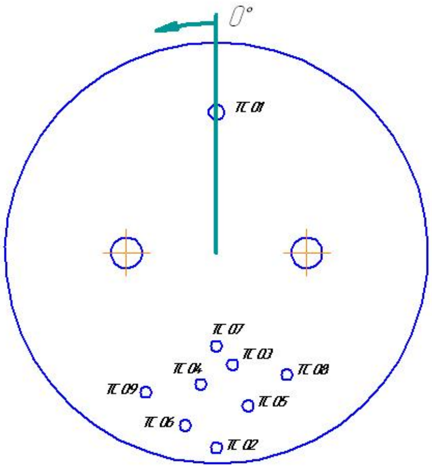

Fig. 2.2 – Location of thermocouple junctions

Table 2.1 – Location of thermocouple junctions

№	**α, º**	**Distance from the axis, mm**	**r, mm** (distance from the specimen axis to hot junction)	**h, mm** (distance from the specimen bottom edge to hot junction)
TC-01	0	0	18	30
TC-02	180	0	25	30
TC-03	188	+2	14.5	30
TC-04	172.2	-2	17	30
TC-05	191.5	+4	20	30
TC-06	169.8	–4	22.5	30
TC-07	180	0	12	30
TC-08	210	+9	18	30
TC-09	153.3	–9	20	30

To charge the furnace with metallic components a stainless steel ring was made, it had an inner diameter of 56 mm, and outer diameter of 94 mm. The ring walls had holes for charge placement (Fig. 2.3). The charging procedure was as follows: 3 mm layer of charged oxidic material was put on the calorimeter. After that the stainless steel charge-ring was put on the specimen. The gap between the crucible and charge was filled with oxidic charge up to the height of the ring. Further on metallic components of the charge were put into the ring holes.

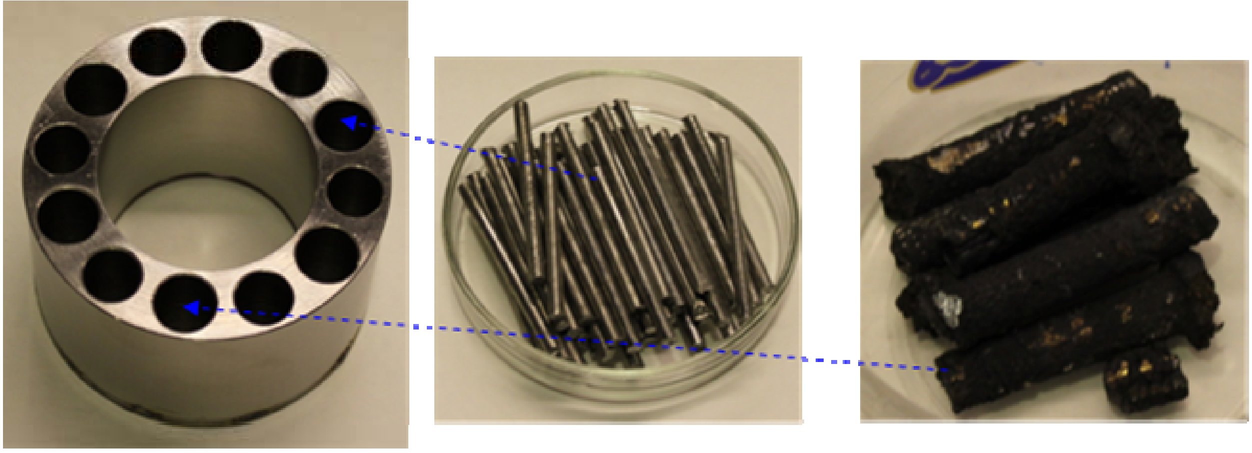

SS **Zr** **U**

Fig. 2.3 – Furnace charge schematics

Gas-aerosol system schematics is given in Fig. 2.4. High-purity Ar (1) was supplied to maintain inert atmosphere in the furnace. The atmosphere was monitored by the electrochemical oxygen sensor (6). During the experiment the furnace was kept under the Ar excess pressure. Petrianov filter of medium area (4) was used to collect aerosols. To control the gas flow parameters (pressure and temperature) the Motorolla pressure transducers and L-type thermocouples were mounted in the points indicated in the scheme. Silica gel column (2) was placed at the furnace inlet to remove traces of moisture from the supplied gas.

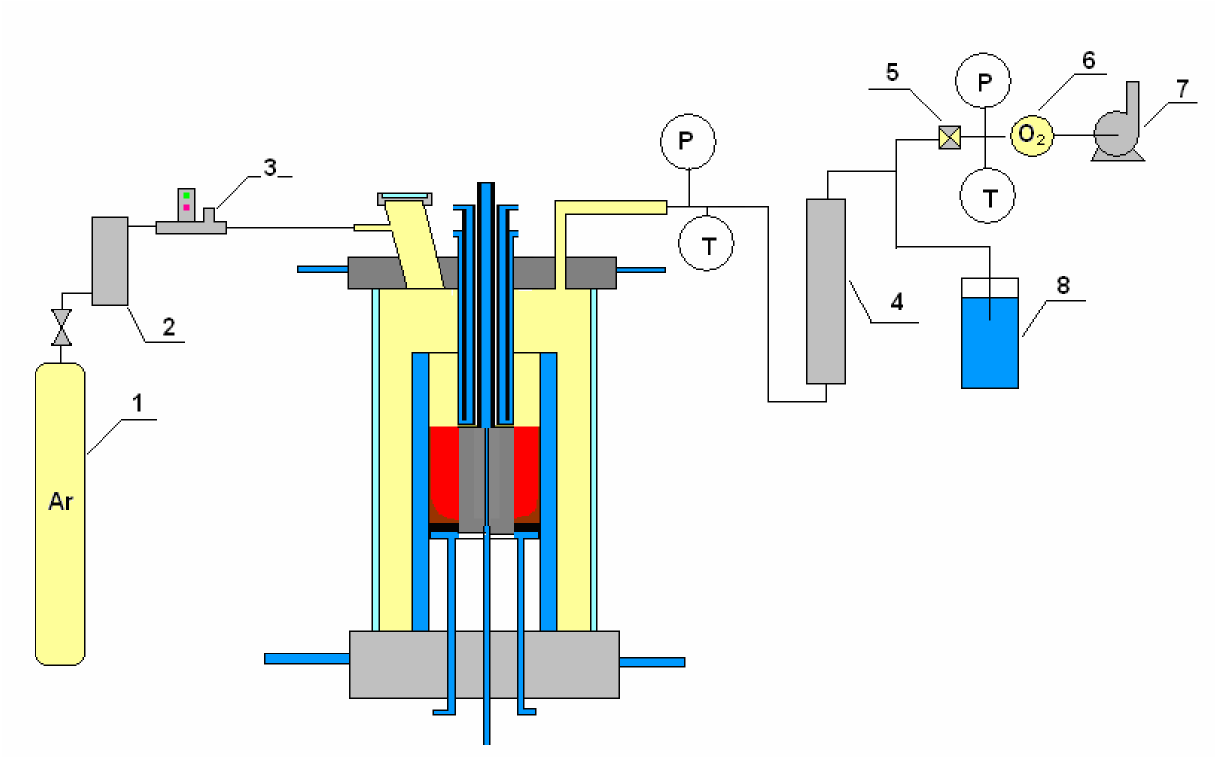

1 –Ar tank; 2 – silica gel dehumidifier; 3 – flow-rate meter-regulator; 4 – Petrianov filter (LAF); 5 – AFA filter; 6 – electrochemical oxygen sensor; 7 – vacuum pump; 8 – hydro lock.

Fig. 2.4 – Gas-aerosol system schematics

2.2. Materials

The following materials were used in the experiment: vessel steel 15Kh2NMFA-A, steel 08Kh18N10T, U and Zr, UO_2, ZrO_2, high-purity argon. Metallic components, steel 08Kh18N10T and vessel steel 15Kh2NMFA-A were analyzed for the content of the main substance. Additionally to that the uranium oxide powder was subjected to the thermogravimetry analysis to evaluate the oxygen/uranium ratio, which was 2.24. Table 2.2. gives the corium charge composition.

Table 2.2 – Composition and mass of the corium charge components

Item	**Content, mass%**									**Mass, g**
	U	**Zr**	**Fe**	**Cr**	**Ni**	**Mn**	**Si**	**Ti**	**Nb**	
Steel 08Kh18N10T[1]	–	–	69.360	17.900	10.400	1.310	0.550	0.480	–	**1005.36**
U[1]	97.300	2.700	–	–	–	–	–	–	–	**819.56**
Zr[1]	–	99.000	–	–	–	–	–	–	1.000	**286.49**
Item	**Mass, g**									
Steel 08Kh18N10T	–	–	697.318	179.959	104.557	13.170	5.529	4.826	–	
U	797.432	22.128	–	–	–	–	–	–	–	
Zr	–	283.625	–	–	–	–	–	–	2.865	
Total, g	**797.432**	**305.753**	**695.508**	**179.959**	**104.557**	**13.170**	**5.529**	**4.826**	**2.865**	

Note:

[1] – composition was determined from the data of X-ray fluorescence analysis (XRF).

The elemental analysis of witness-specimen and molten products was made by the X-ray fluorescence analysis (XRF) on the vacuum spectrometer Spectroscan MAX-GV. Vessel steel witness-specimen as a ≈15 mm-diameter disk was cut from the steel cylinder by a lathe.

Table 2.3 gives the XRF data of the vessel steel witness-specimen in comparison with the Technical specifications (TS) for the vessel steel of this brand.

Table 2.3 – XRF data on the vessel steel witness-specimen

TS, analysis method	**Content of chemical elements, % mass**												
	Al	**C**	**Si**	**Mn**	**Cr**	**Ni**	**Mo**	**V**	**P**	**S**	**Cu**	**Co**	**As**
TS 108-765-78		0.13÷0.18	0.17÷0.37	0.30÷0.60	1.8÷2.3	1.0÷1.5	0.5÷0.7	0.10÷0.12	<0.02	<0.02	<0.3	<0.03	<0.003
XRF	0.356	–	0.193	0.440	2.08	1.14	0.518	0.096	–	–	0.234	–	0.002

The available XRF data confirm the identity of the 15X2NMFA-A steel used in the experiment with the composition mentioned in the TS 108-765-78.

2.3. Experimental procedure

After the furnace charging it was flushed with argon for 5 minutes at a 10 l/min flow rate in order to remove air absorbed by charge powder and establish the inert atmosphere. After that the HF heating was turned on. Until 5110 s the metallic charge was gradually heated and molten, the inductor voltage was stepped up from 5110 to 7200 s until 1400ºC was reached in the specimen surface (in accordance with TC02). From that time the stable temperature of 1400ºC was maintained by adjusting voltage vs. the thermocouple readings. Fig. 2.6 gives the heat and electromagnetic fluxes into the cold crucible, specimen and bottom calorimeter versus time.

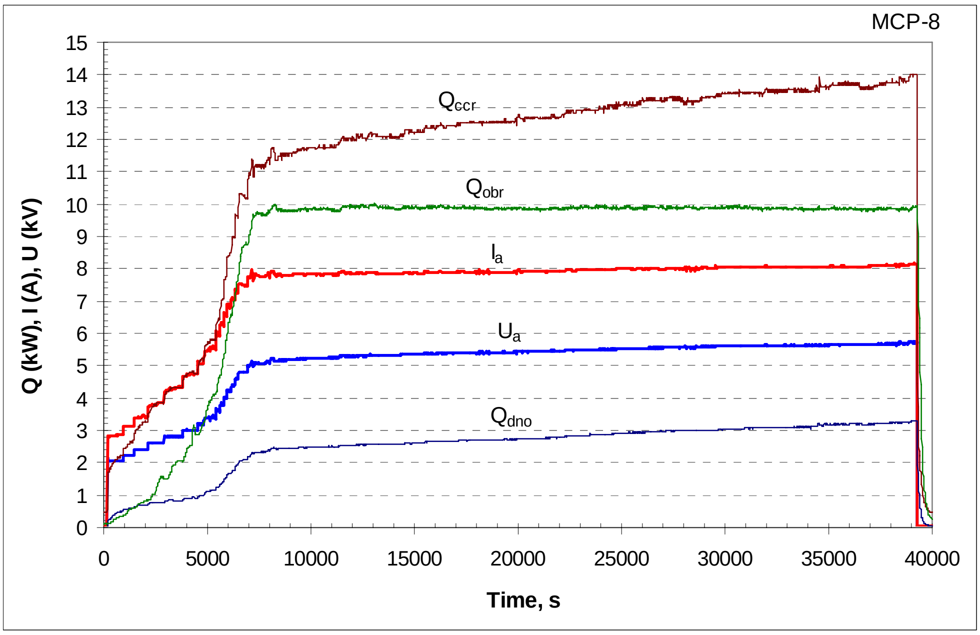

Fig. 2.5 – Heat flux into the cold crucible Q_{ccr}, specimen Q_{obr} and bottom calorimeter Q_{dno} versus time

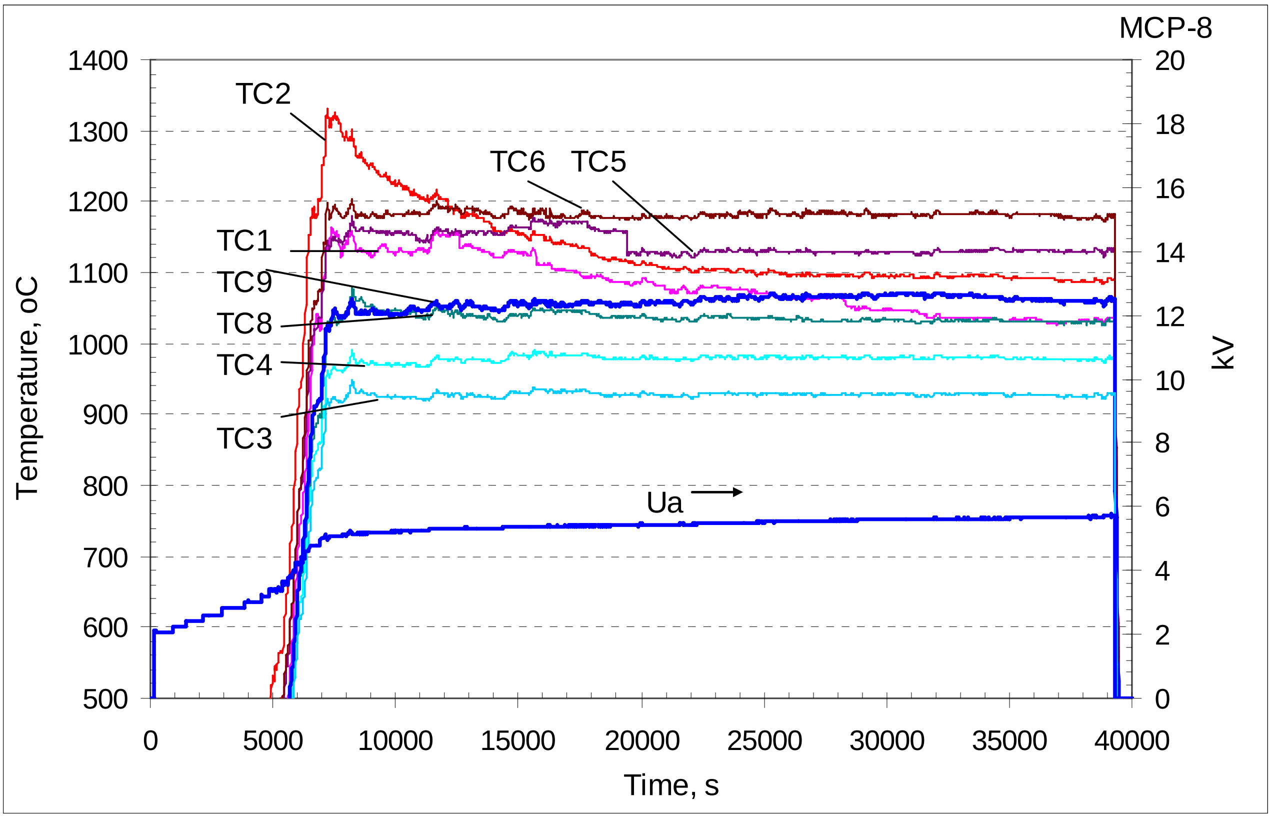

Fig. 2.6 – Thermocouple readings

During a long-term exposition at a rather high temperature level a number of thermocouples broke down. Due to ablation some thermocouple junctions got out of the specimen body to the crust or melt, and the thermocouples could produce new false junctions. For this reason the analysis used only the data from thermocouples, hot junctions of which remained in the uncorroded part of the specimen.

2.4. Ultrasonic measurement of specimen corrosion

The ultrasonic sounding method was used to measure the corrosion depth, i.e. the change of interaction front position versus time. The specimen was sounded by the periodic-pulse signal. Between pulses the ultrasonic transducer is automatically switched to the regime of echo-signal receiving. The distance between reflecting surfaces (specimen surface and acoustic defect):

$$D = 0.5c\Delta t, \qquad (2.1)$$

where c – speed of sound in the specimen;

Δt – time interval between radiated and reflected echo-signals.

Fig. 2.7 shows the image of echo signals on the monitor, it looks like the two groups of sinusoidal signals. The left group corresponds to the signal from acoustic defect, and the right – from the specimen surface. The main oscillation frequency – own resonance frequency of ultrasonic transducer. The spectral composition of groups differs due to different shapes of reflecting surfaces.

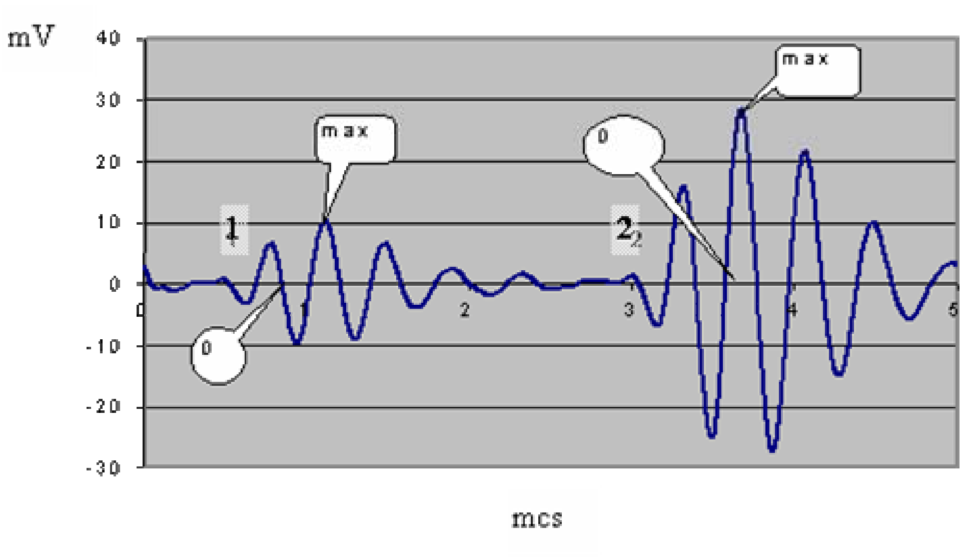

1 – echo signal from defect; 2 – echo signal reflected from the specimen surface; «max» – positions of synphased half-waves maxima; «0» – positions of synphased halfwave zero points

Fig. 2.7 – Specimen echogram

Fig. 2.8 shows the processed ultrasonic measurements. The accuracy of the measurements can be judged by the ratio between the corrosion depth registered by the end of the experiment - ≈9.5 mm and the directly measured value of the posttest axial section (profilogram of Fig. 3.5). This value is approximately 9.0 mm.

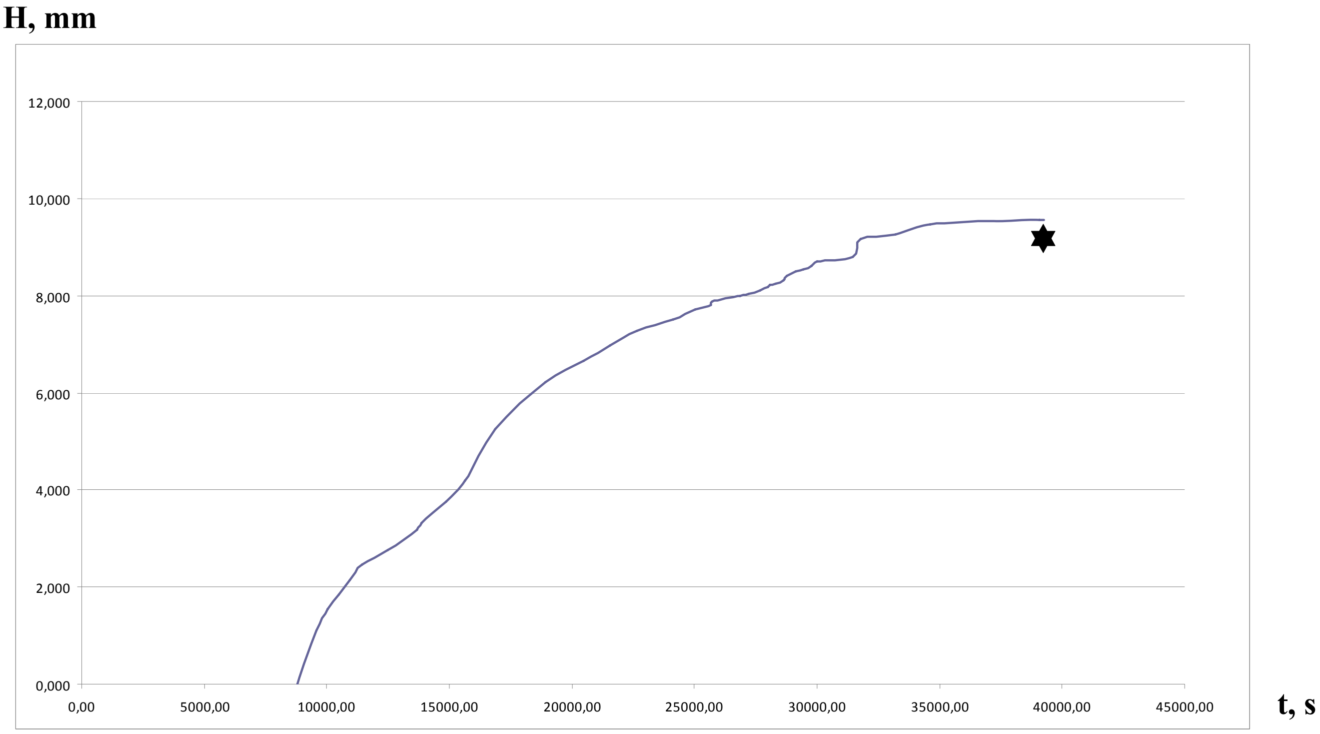

✡ – posttest measurements; —– ultrasonic measurements

Fig. 2.8 – Specimen corrosion depth versus time

3. POSTTEST ANALYSIS

3.1. Ingot macrostructure

At the furnace disassembling a crust was found on the corium ingot surface (Figs 3.1, 3.2), its thickness was 2÷3 mm. The ingot height (Fig. 3.2) was approximately 50 mm.

Ingot with the steel specimen was taken out of the crucible, and corium ingot separated from the specimen. After that the specimen with the crystallized melt, which got stuck to it, was included into the epoxy resin. The frozen matrix with the specimen was cut along the axis (Fig. 3.3), one of the separated halves was used to make a polished section for the SEM/EDX analysis.

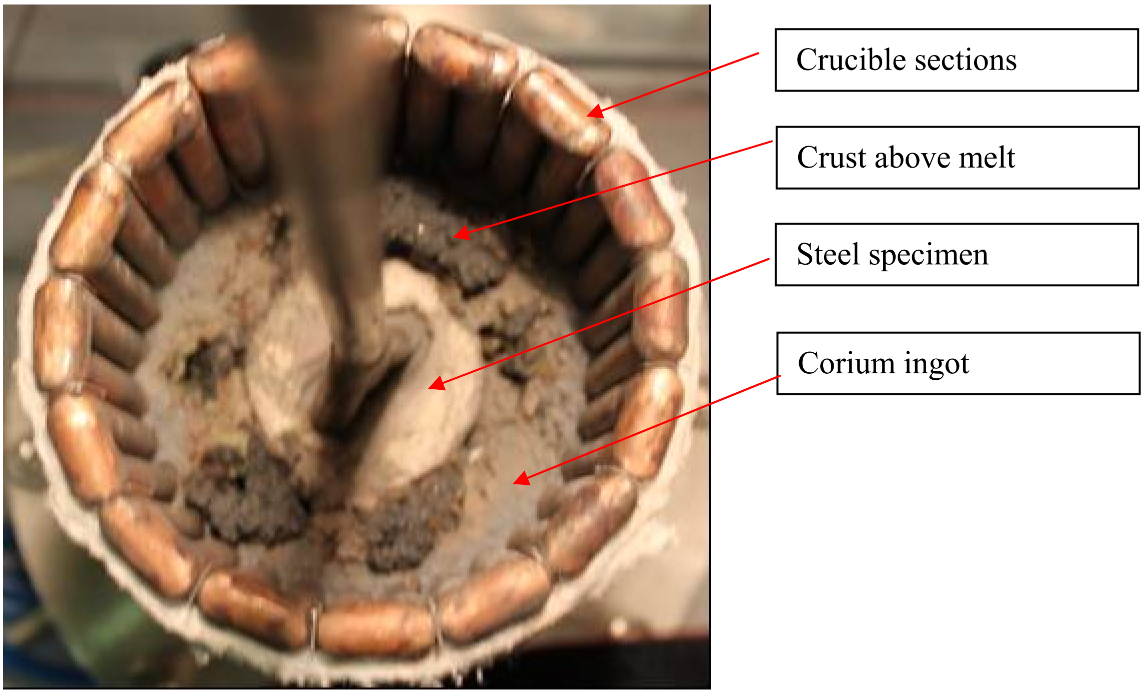

Fig. 3.1 – Crucible after the experiment

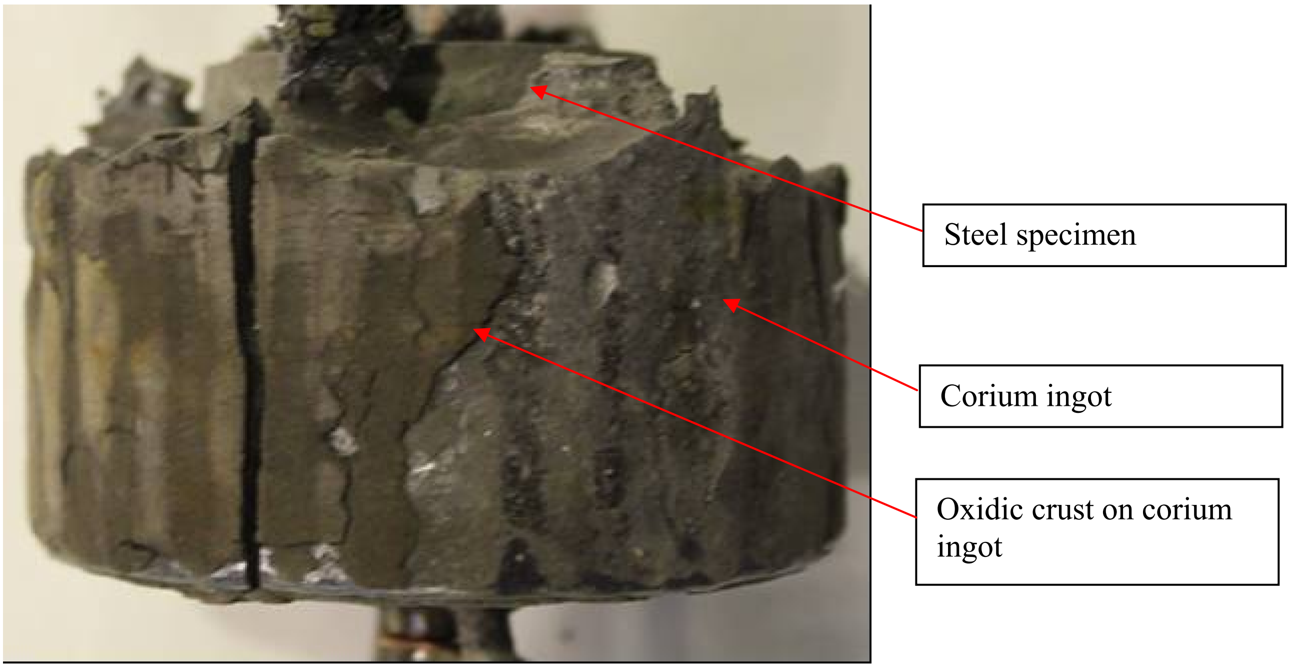

Fig. 3.2 – Ingot with the steel specimen after extraction from the crucible

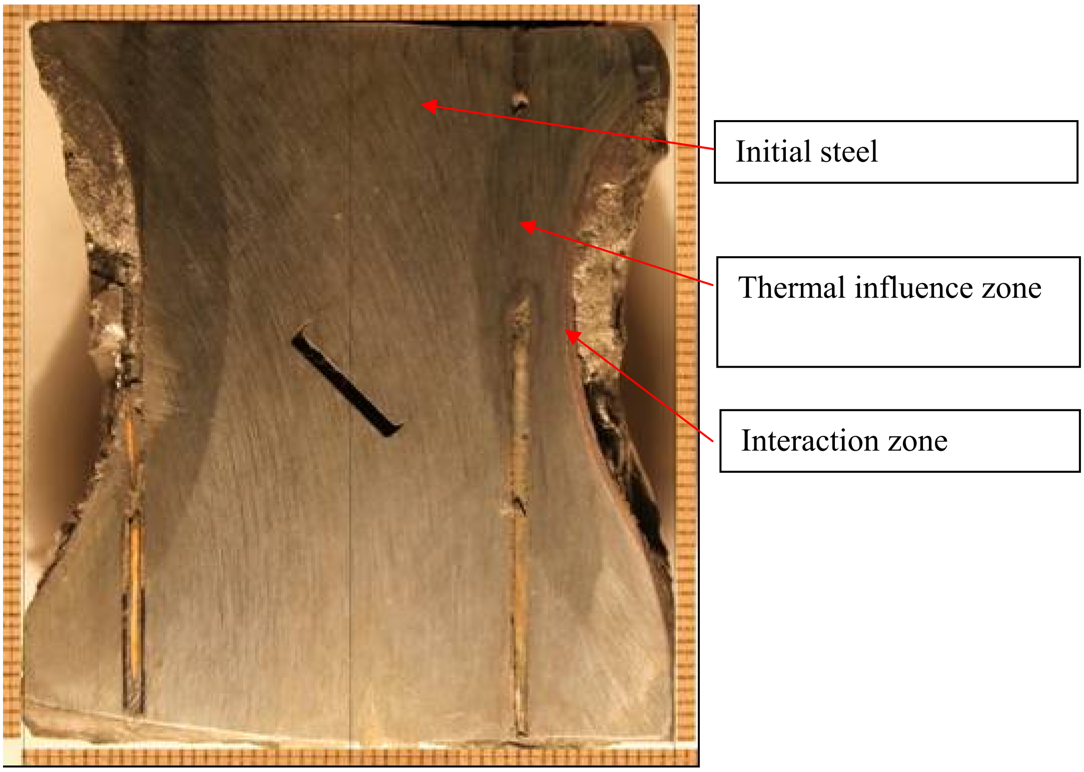

Fig. 3.3 – Axial section of the steel specimen

Fig. 3.4 shows the axial section with a corium part, which got stuck to it.

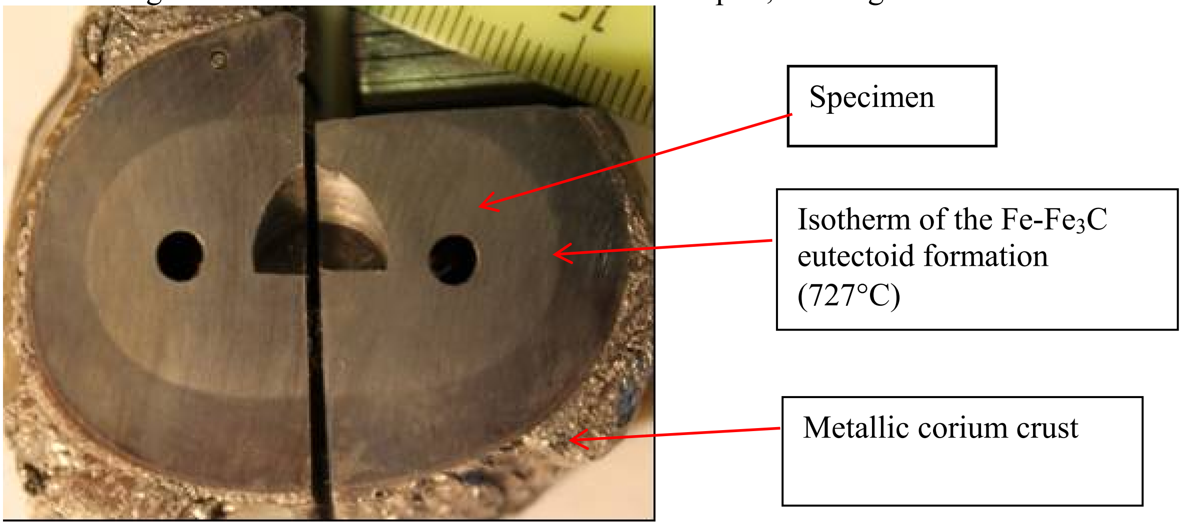

Fig. 3.4 – Specimen cross section (reconstructed)

Fig. 3.5 shows the specimen profilograms of the axial and cross sections constructed using the measured data. They show the thermal influence zones – isotherm of a Fe – Fe_3C eutectoid formation (727ºC).

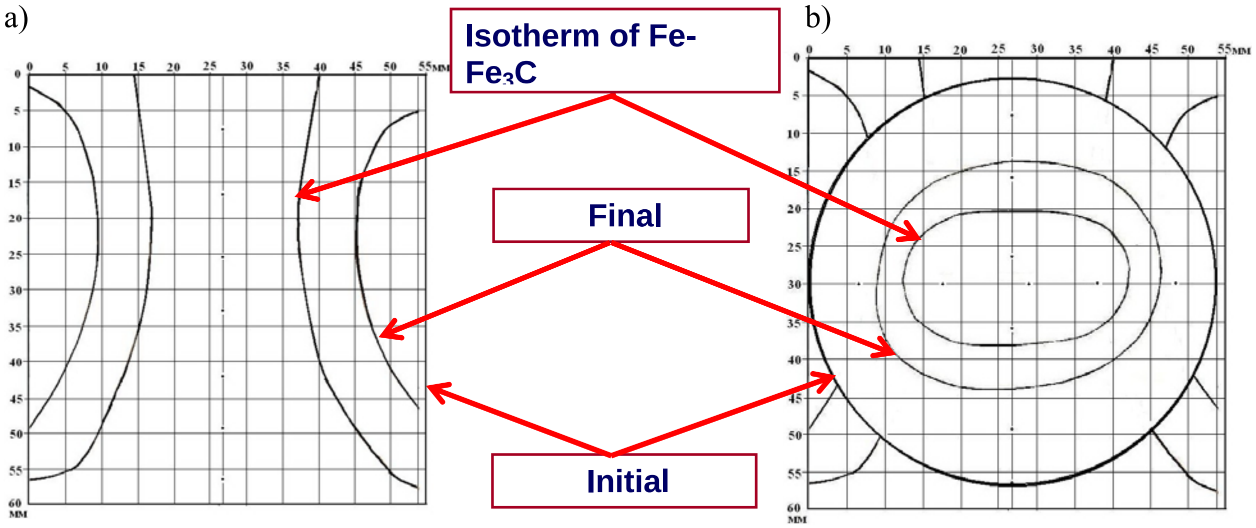

a – axial section; b – cross section

Fig. 3.5 – Profilograms of specimen sections

3.2. Numeric modeling of the specimen temperature conditions

To determine conditions, in which the steel corrosion was progressing and, most important, ceased, the specimen temperature conditions were calculated. The data were used in the resulting analysis of experimental data. The calculations were made in the standard 3D formulation using the ANSYS code. The boundary conditions were as follows: temperatures on the internal surfaces of the specimen cooling channels (100°C), calorimeter (100°C), s screen-shaft (20°C), which was separated from the periphery part of the specimen top by the ZrO_2 plate. In the calculations the heat flux to the specimen side surface was varied to get the best convergence of numeric and experimental temperature values in locations of thermocouple junctions, as well as for the agreement of calculated temperature on the boundary of the thermal influence zone with the temperature of the eutectoid formation in the Fe – Fe_3C (727ºC) system.

Fig. 3.6÷3.8 shows the calculated distribution of temperature in the specimen, and Fig. 3.9 – comparison of calculations with measured temperatures. Figs. 3.7, 3.8 show the 727ºC isotherm (see profilogram in Fig. 3.5), deviation from the calculation was ≈30ºC, and a difference with thermocouple measurements (Fig. 3.9) did not exceed 50ºC.

In accordance with calculations the temperature on the final boundary of specimen ablation is 1050÷1150ºC. A large scattering is explained by the necessity of the 3D modeling.

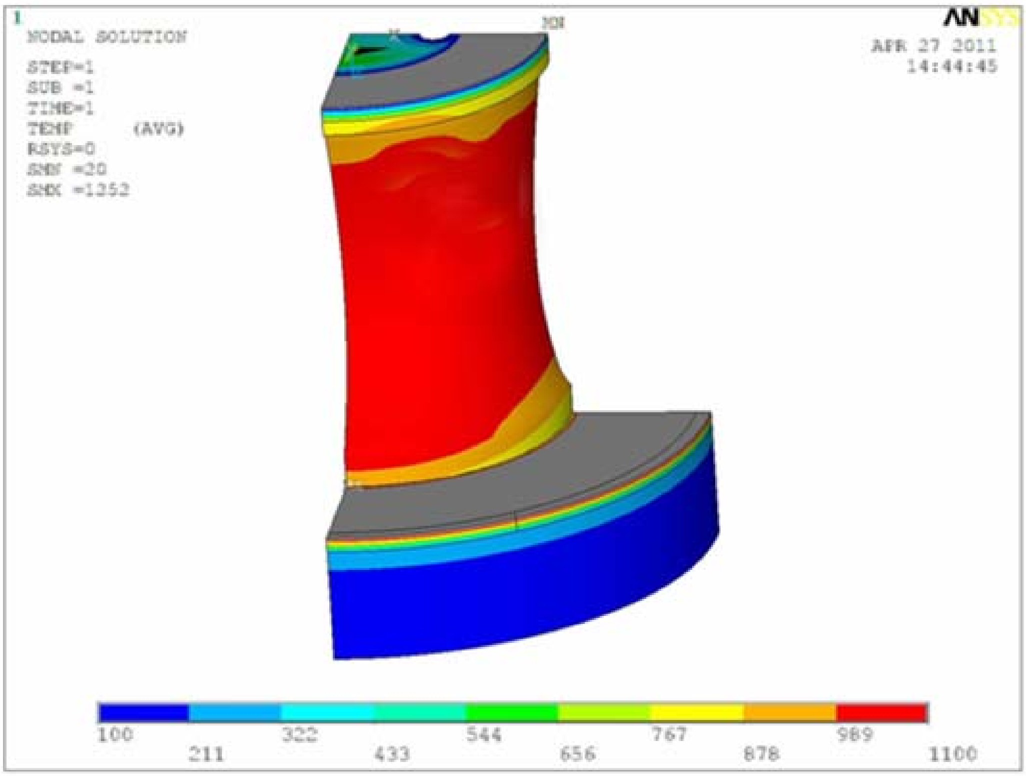

Fig. 3.6 – Temperature distribution on the outside specimen surface

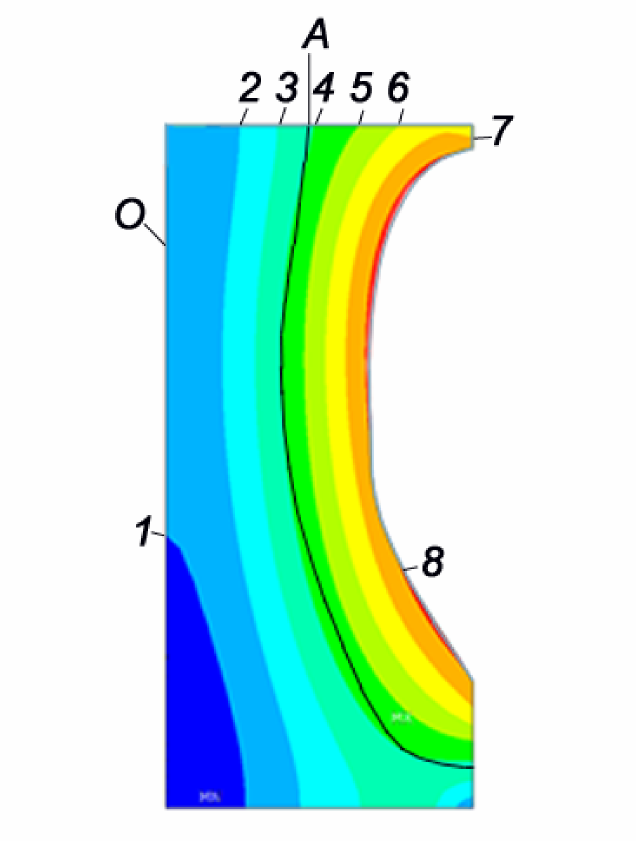

O – specimen axis

A – isotherm of the Fe-Fe$_3$C eutectoid formation (727°C); 1 – 400; 2 – 500;
3 – 600; 4 – 700; 5 – 800; 6 – 900; 7 – 1000; 8 – 1100°C

Fig. 3.7 – Temperature field in the longitudinal specimen section (the symmetry plane between the cooling channels)

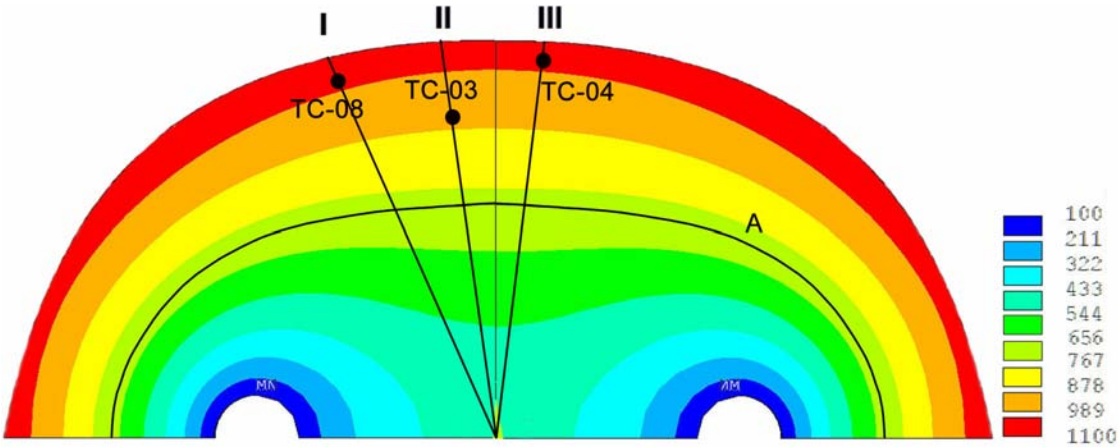

Fig. 3.8 – Temperature field in the specimen cross-section

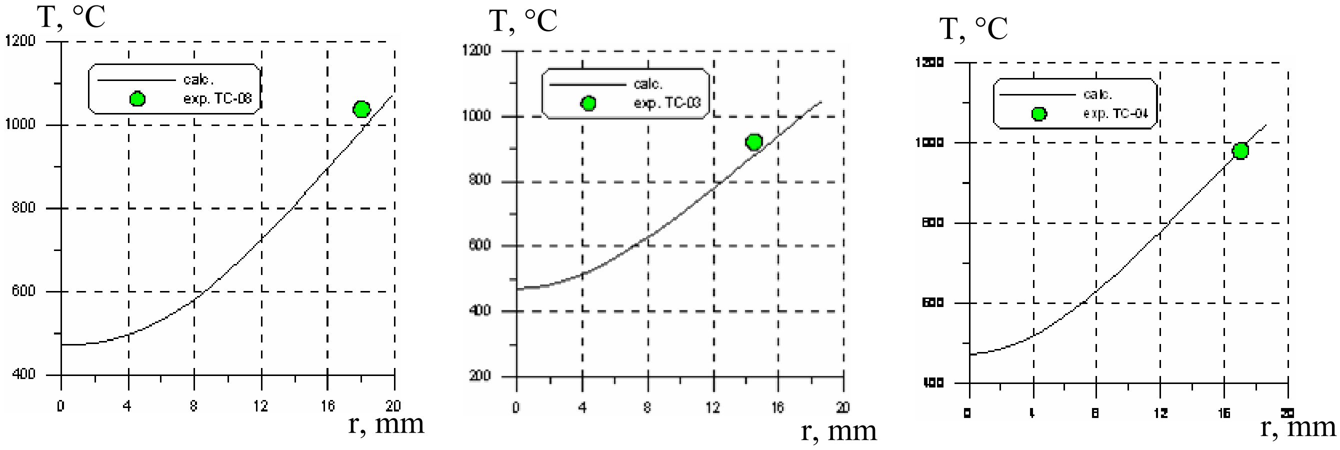

Fig. 3.9 – Comparison of calculations with thermocouple measurements (location of thermocouples in Fig. 3.8)

3.3. Physicochemical analysis

3.3.1. Material balance of the experiment

To make the material balance the initial charge components and molten products were weighed with an accuracy up to 0.01 g, after that they were analyzed for the content of main components.

Table 3.1 gives the material balance of MCP-8.

Table 3.1 –MCP-8 material balance

Introduced into the melt, g		Collected after the experiment, g	
Steel 08Kh18N10T	1005.36	**Above-melt crust**	133.44
U	819.56	**Ingot**	2042.07
Zr	286.49	**Aerosols**	0.27
Σ	**2111.41**	Σ	**2175.51**
Imbalance	**+64.10**		

3.3.2. X-ray fluorescence analysis

The elemental analysis of metallic ingot, above-melt crust was performed by XRF using the vacuum spectrometer Spectroscan MAKS-GV [3]. To determine the content of elements in molten products the methods of regression analysis and of fundamental parameters were used.

The regression analysis is one of the methods for the quantitative XRF using the "Spectr-Quant" software. It calculates the concentration of elements by the method of multiple regression from the intensity of their characteristic X-ray lines measured at the analysis, taking into account coefficients of graduation equations calculated at the calibration of the X-ray spectrometer. In this analysis the drift of the spectrometer instrumental characteristics was taken into account by the measured reference specimen, and different methods for taking the background into account were used (from points, lines of non-coherent dissipation, blank sample). When the regression analysis was used, the XRF error on the U and Zr content did not exceed 5 rel.%.

The method of fundamental parameters (MFP) is the qualitative and quantitative reference (and reference-free) X-ray fluorescence based on theoretical correlations describing physical processes of X-ray fluorescence excitation in the specimen accompanied by its registration by the spectrometer. The program is tuned on a concrete spectrometer using the high-quality calibration specimens covering the whole operation range (all crystals and wavelengths). The MFP enables to calculate concentrations of practically any inventory of evaluated elements in the studied specimen without calibration samples. The relative errors of quantitative analysis without a reference sample depend on the content of determined elements; they are:

- in the range from 0.1 to 1.0 % mass – ≈20 % rel.,
- in the range from 1.0 to 5.0 % mass – 3÷5 % rel.,
- in the range from 5 to 10 % mass – 1÷3 % rel.,
- in the range from 30 % mass – 0.5÷2 % rel.

When reference samples are used the accuracy of quantitative analysis by the MFP is not worse than that of regression analysis.

The crust was crushed to the particle size > 200 µm, from it an average sample was prepared by quartering, and it underwent a further grinding to the particle size < 50 µm, following that it was subjected to analysis. The sample was prepared for analysis in the argon atmosphere.

From the ¼ part of metallic ingot three samples were cleaved, and from them polished sections for the XRF were prepared.

The XRF data and elemental material balance are presented in Table 3.2.

Table 3.2 – MCP-8 XRF data of molten products and elemental mass balance

Item	**Content, mass%**										**Mass, g**
	U	**Zr**	**Fe**	**Cr**	**Ni**	**Mn**	**Si**	**Ti**	**Nb**	**Mo**	
Above-melt crust	57.518	19.216	16.369	3.772	2.014	0.289	0.326	0.342	0.113	0.041	**133.44**
Ingot (top)	34.946	13.788	38.039	8.895	5.332	0.652	0.256	0.22	0.131	0.014	**2042.074**
Ingot (center)	35.379	13.779	36.98	8.11	4.51	0.623	0.261	0.206	0.139	0.013	
Ingot (bottom)	35.536	13.577	37.165	8.887	5.231	0.644	0.252	0.215	0.130	0.014	
***Ingot (average sample)*1)**	*35.287*	*13.715*	*36.099*	*8.631*	*5.024*	*0.640*	*0.256*	*0.214*	*0.133*	*0.014*	
Aerosols2)	–	–	–	–	–	–	–	–	–	–	**0.27**
Item	**Mass, g**										
Crust	76.752	25.642	21.843	5.033	2.687	0.386	0.435	0.456	0.151	0.055	
Ingot	720.587	280.064	737.161	176.245	102.601	13.062	5.235	4.363	2.723	0.279	
Collected, g	797.338	305.706	759.004	181.278	105.288	13.448	5.669	4.820	2.873	0.334	
Introduced, g	797.432	305.753	697.318	179.959	104.557	13.170	5.529	4.826	2.865	–	
Imbalance, g	–0.09	–0.05	+61.69	+1.32	+0.73	+0.28	+0.14	+0.01	+0.01	+0.33	
% from introduced	0.01	0.02	–	–	–	–	–	–	–	–	

Notes:

1) – Mass calculated from the average sample.

2) – Aerosols were not analyzed due to small quantity.

It can be seen from Table 3.2. that at the interaction of metallic melt with vessel steel approximately 64.5 g of vessel steel (incl. 61,7 g of iron) partitioned into the melt. This value approximately corresponds to the mass of dissolved steel evaluated from the reduction of specimen volume.

3.3.3. Chemical analysis

The above-melt crust was analyzed for the content of U, Zr and Fe ions. The average sample was used, which was taken by quartering and crushed to the particle size < 50 µm. All preparations were made in the argon atmosphere.

The specimens for analysis were prepared by the fusion of 0.1÷0.5 g samples taken from the ingot and other molten products with (3.0±0.5) g potassium pyrosulphate at 900±25°C up to the production of transparent melt, which was later dissolved at heating in the 200÷250 ml of 1M solution of sulfuric acid.

After that Zr was evaluated by photometry as Zr^{4+} with xylenol orange [4÷7], uranium as U^{+4} – with reagent arsenazo III [8÷10] and iron as Fe^{+2} – with orthophenanethroline [7, 11].

Table 3.3 gives the results of chemical analysis.

Table 3.3 – Chemical analysis of molten products

Item	Content, mass%		
	U	Zr	Fe
Above-melt crust	58.02	18.24	15.62

The comparison of the above-melt crust compositions made by XRF (Table 3.2) and chemical analysis (table 3.3) shows their good agreement.

3.4. SEM/EDX analysis

Two polished sections were prepared for the SEM/EDX analysis (top and bottom), they represent a quarter of the specimen axial section. The polished sections demonstrate an even boundary of steel degradation, which corresponds to the temperature field established in the system. The crystallized melt adjacent to the non-degraded steel is not separated from the upper polished section, in the lower polished section it is separated from steel by the shrink crack.

Fig. 3.10 shows the regions of ingot and steel specimen, which were subjected to the SEM/EDX analysis. The SEM-images are shown in the figures below, and corresponding data of the EDX analyses– in tables.

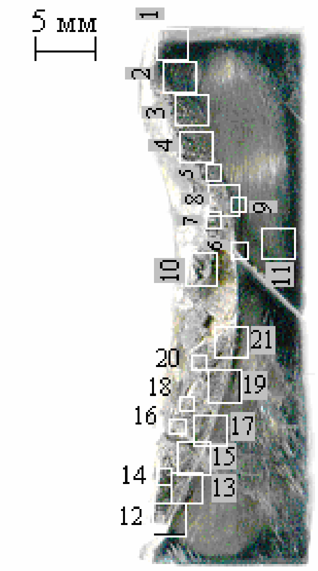

Fig. 3.10 –MCP-8 polished sections with regions marked for the SEM/EDX studies

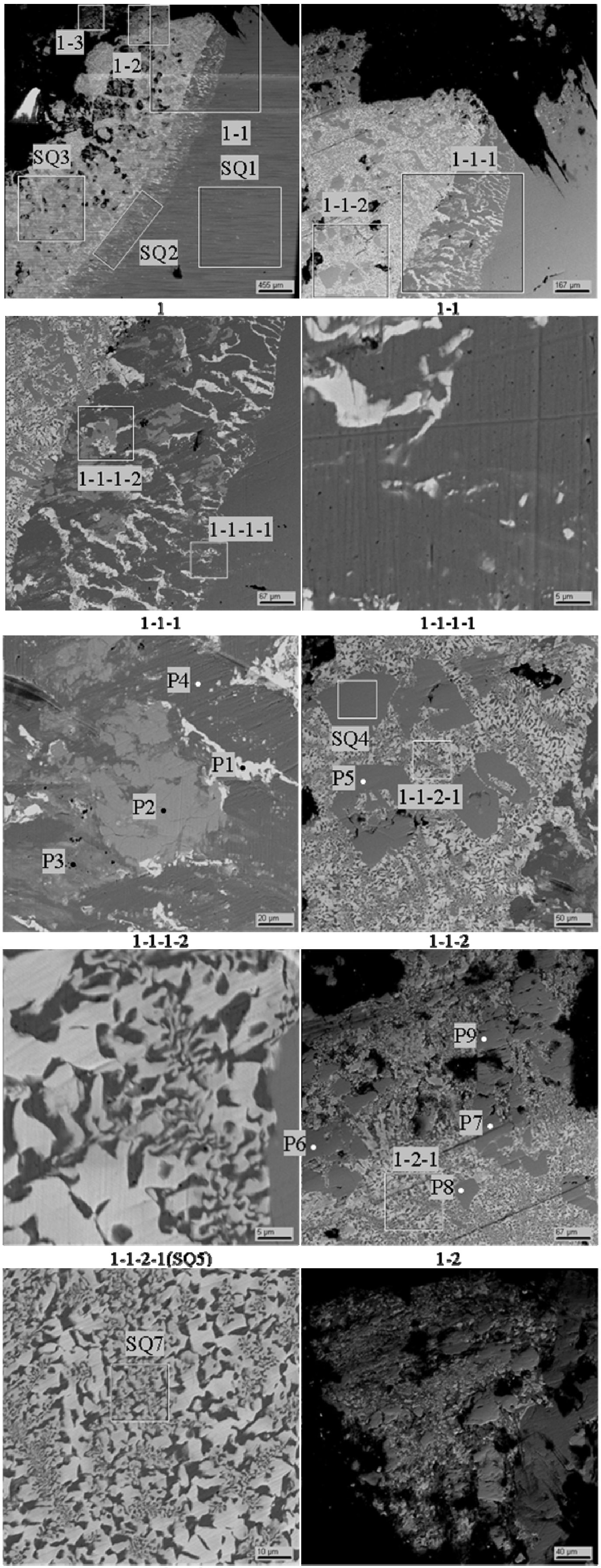

1 1-1

1-1-1 1-1-1-1

1-1-1-2 1-1-2

1-1-2-1(SQ5) 1-2

1-2-1 (SQ6) 1-3

Fig. 3.11 – Microphotograph of Region 1

Table 3.4 – EDX data of Region 1

№		U	Zr	Fe	Cr	Ni	Si	Phase
SQ1	mass%	1.7	0.5	93.5	3.0	1.0	0.2	–
	mol.%	0.4	0.3	94.6	3.2	1.0	0.4	
SQ2	mass%	20.9	7.4	59.8	9.0	3.0	–	–
	mol.%	6.0	5.6	73.2	11.8	3.5	–	
SQ3	mass%	24.5	13.0	51.4	7.5	3.6	–	–
	mol.%	7.5	10.4	67.1	10.4	4.5	–	
SQ4	mass%	8.2	25.4	57.9	5.5	2.9	–	$ZrFe_3$ crystal
	mol.%	2.3	18.5	68.8	7.1	3.3	–	
SQ5	mass%	31.7	11.3	46.9	6.7	3.4	–	«light» eutectics
	mol.%	10.4	9.7	65.4	10.0	4.6	–	
SQ6	mass%	30.7	5.9	51.3	7.6	4.6	–	
	mol.%	9.6	4.8	68.8	10.9	5.9	–	
SQ7	mass%	30.6	6.3	51.3	7.9	3.9	–	
	mol.%	9.6	5.1	68.8	11.4	5.0	–	
P1	mass%	53.8	5.0	34.3	1.9	5.0	–	UFe_3
	mol.%	22.2	5.4	60.4	3.7	8.4	–	
P2	mass%	51.1	14.0	22.9	10.7	1.4	–	$(U,Zr)(Fe,Cr)_2$
	mol.%	21.3	15.2	40.7	20.4	2.4	–	
P3	mass%	14.0	1.0	73.0	9.1	2.9	–	Mixture of phases
	mol.%	3.7	0.7	81.6	11.0	3.1	–	
P4	mass%	4.2	2.3	77.4	14.1	1.9	–	
	mol.%	1.0	1.5	79.9	15.7	1.9	–	
P5	mass%	7.0	28.5	56.6	5.3	2.6	–	$ZrFe_3$
	mol.%	2.0	20.8	67.5	6.8	3.0	–	
P6	mass%	7.1	27.9	56.8	5.2	2.9	–	
	mol.%	2.0	20.4	67.7	6.7	3.3	–	
P7	mass%	7.8	28.6	54.9	5.6	3.1	–	
	mol.%	2.2	21.0	66.0	7.2	3.6	–	
P8	mass%	7.6	25.0	57.5	6.1	3.8	–	
	mol.%	2.1	18.1	67.8	7.7	4.3	–	
P9	mass%	7.4	31.5	52.4	5.5	3.1	–	
	mol.%	2.1	23.4	63.7	7.2	3.6	–	

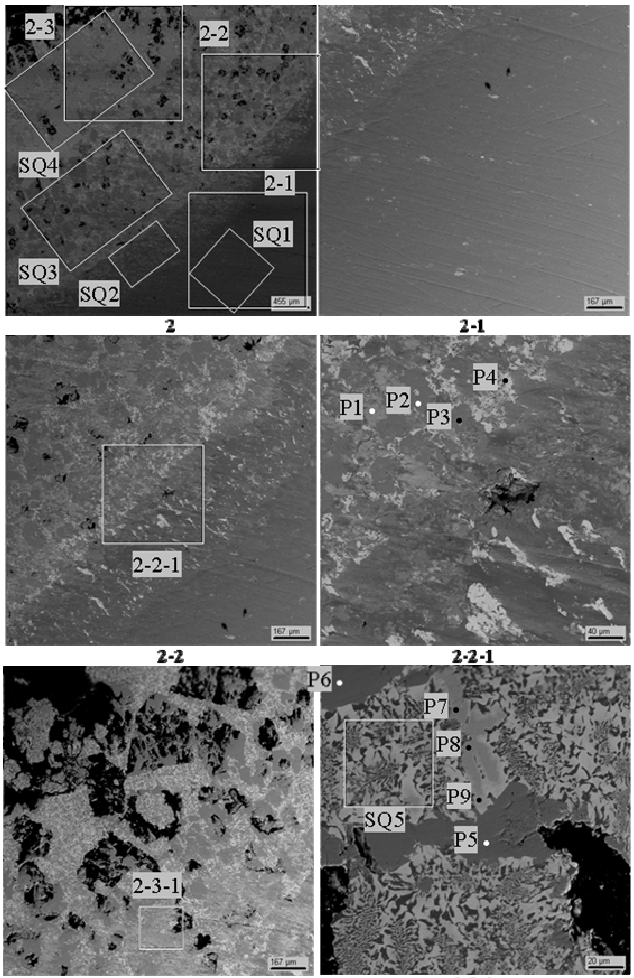

2 2-1
2-2 2-2-1
2-3 2-3-1

Fig. 3.12 – Microphotographs of Region 2

Table 3.5 – EDX data of Region 2

№		U	Zr	Fe	Cr	Ni	Phase
SQ1	mass%	3.6	1.2	90.8	2.9	1.6	–
	mol.%	0.9	0.7	93.7	3.2	1.5	
SQ2	mass%	20.9	10.7	56.7	9.1	2.6	–
	mol.%	6.1	8.1	70.5	12.2	3.1	
SQ3	mass%	24.3	16.2	49.5	6.5	3.5	–
	mol.%	7.6	13.1	65.7	9.3	4.4	
SQ4	mass%	24.4	22.0	43.9	4.9	4.7	–
	mol.%	7.9	18.5	60.2	7.3	6.2	
SQ5	mass%	28.6	16.5	43.7	6.7	4.5	«light» eutectics
	mol.%	9.3	14.1	60.7	10.0	5.9	
P1	mass%	34.7	16.6	41.1	3.1	4.5	$(Zr,U)Fe_3$
	mol.%	12.2	15.1	61.3	5.0	6.5	
P2	mass%	10.1	23.7	56.5	6.3	3.4	$ZrFe_3$
	mol.%	2.8	17.4	67.8	8.1	3.9	
P3	mass%	37.7	13.0	36.8	10.1	2.5	$(U,Zr)Fe_3$
	mol.%	13.2	11.9	55.1	16.2	3.6	
P4	mass%	48.8	10.0	33.9	2.3	5.1	Mixture of phases
	mol.%	19.5	10.4	57.7	4.1	8.3	
P5	mass%	20.1	26.3	44.3	4.3	4.9	$ZrFe_3$
	mol.%	6.4	21.6	59.5	6.3	6.3	
P6	mass%	20.4	26.9	43.7	4.5	4.5	
	mol.%	6.5	22.2	59.0	6.6	5.8	
P7	mass%	28.0	15.3	45.6	7.5	3.7	$(Zr,U)(Fe,Cr)_3$

	mol.%	9.0	12.8	62.4	11.0	4.9	
P8	mass%	25.3	17.3	46.8	5.8	4.8	
	mol.%	8.0	14.3	63.1	8.5	6.1	
P9	mass%	35.6	6.9	45.0	7.7	4.7	(U,Zr)(Fe,Cr)$_3$
	mol.%	11.9	6.0	64.0	11.8	6.4	

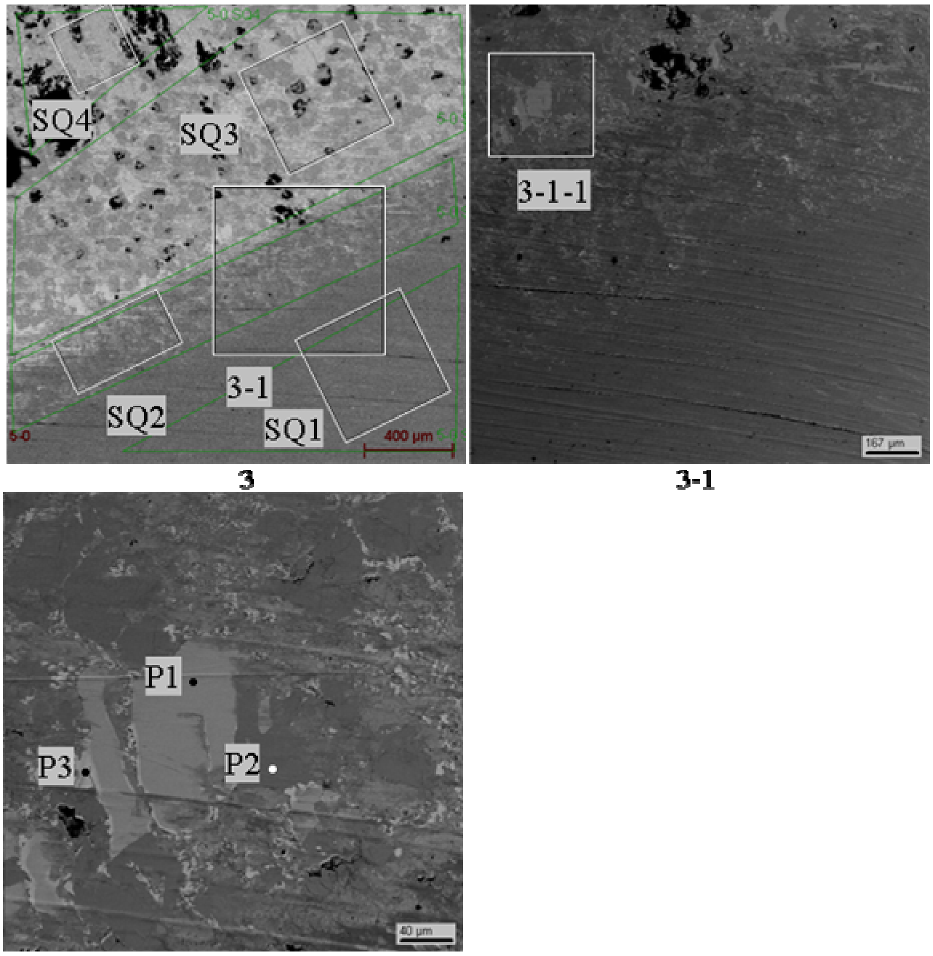

3 3-1

3-1-1

Fig. 3.13 – Microphotographs of Region 3

Table 3.6 – EDX data of Region 3

№		U	Zr	Fe	Cr	Ni	Phase
SQ1	mass%	5.3	2.6	87.3	3.2	1.7	–
	mol.%	1.3	1.7	91.8	3.6	1.7	
SQ2	mass%	15.4	11.2	59.9	11.2	2.4	–
	mol.%	4.3	8.1	70.8	14.2	2.7	
SQ3	mass%	25.7	14.9	49.4	6.5	3.5	–
	mol.%	8.1	12.2	66.0	9.3	4.4	
SQ4	mass%	25.9	18.0	45.4	6.2	4.5	–
	mol.%	8.3	15.0	61.8	9.1	5.9	
P1	mass%	34.9	16.0	41.9	3.0	4.2	(Zr,U)Fe$_3$
	mol.%	12.2	14.6	62.5	4.9	5.9	
P2	mass%	10.0	25.7	54.5	6.3	3.4	ZrFe$_3$
	mol.%	2.9	19.0	66.0	8.2	3.9	
P3	mass%	41.7	13.1	38.9	2.1	4.2	(U,Zr)Fe$_3$
	mol.%	15.5	12.8	61.8	3.6	6.3	

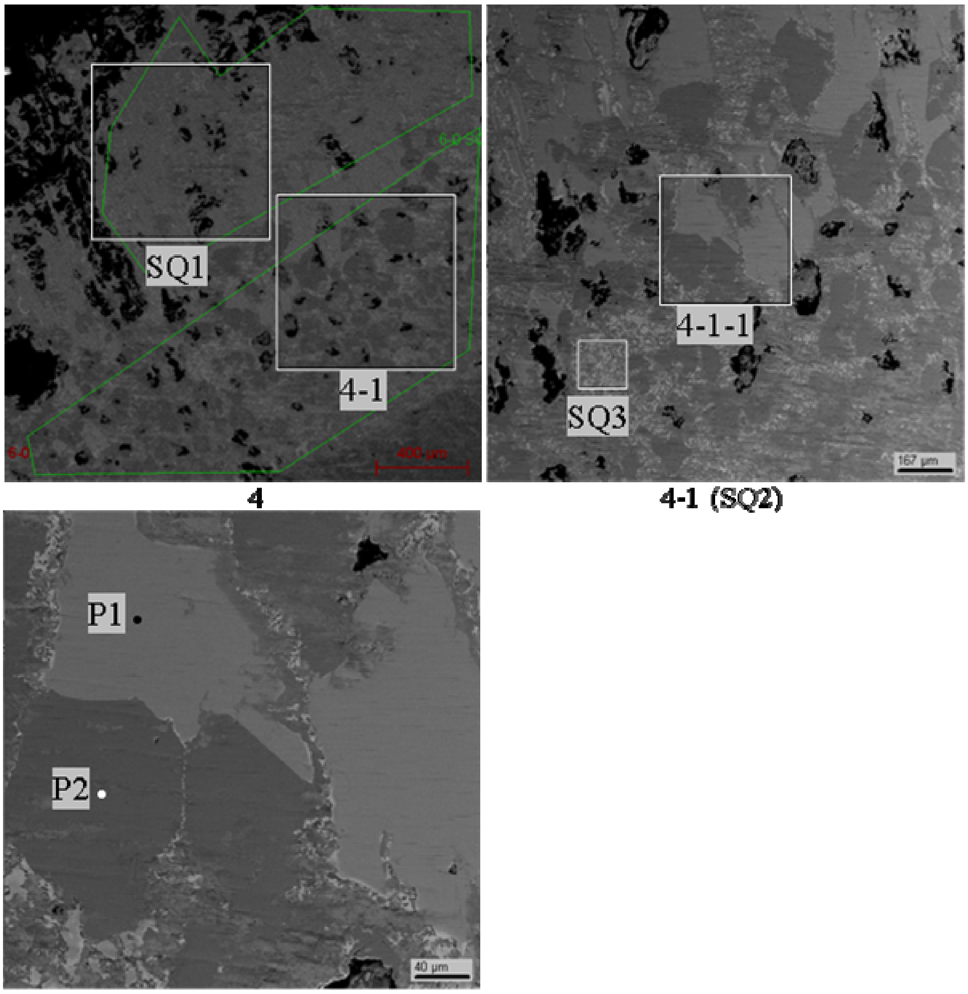

4 4-1 (SQ2)

4-1-1

Fig. 3.14 – Microphotographs of Region 4

Table 3.7 – EDX data of Region 4

№		U	Zr	Fe	Cr	Ni	Phase
SQ1	mass%	24.8	22.5	43.1	5.4	4.1	–
	mol.%	8.0	19.1	59.5	8.0	5.4	
SQ2	mass%	24.8	16.3	48.7	6.5	3.7	–
	mol.%	7.8	13.3	64.9	9.3	4.7	
SQ3	mass%	31.4	12.1	45.4	7.3	3.8	«light» eutectics
	mol.%	10.3	10.4	63.4	11.0	5.0	
P1	mass%	23.9	25.7	42.2	3.9	4.2	$ZrFe_2$
	mol.%	7.8	21.9	58.8	5.9	5.6	
P2	mass%	9.7	25.2	55.6	6.4	3.1	$ZrFe_3$
	mol.%	2.7	18.5	66.9	8.3	3.6	

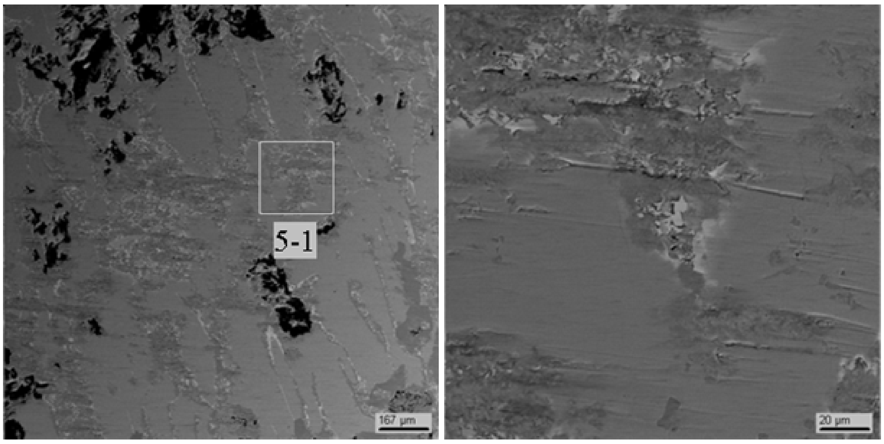

5 5-1

Fig. 3.15 – Microphotographs of Region 5

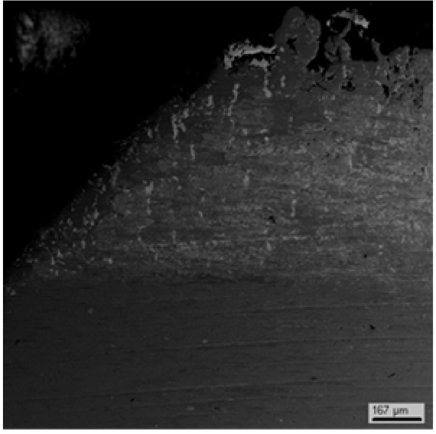

6

Fig. 3.16 – Microphotographs of Region 6

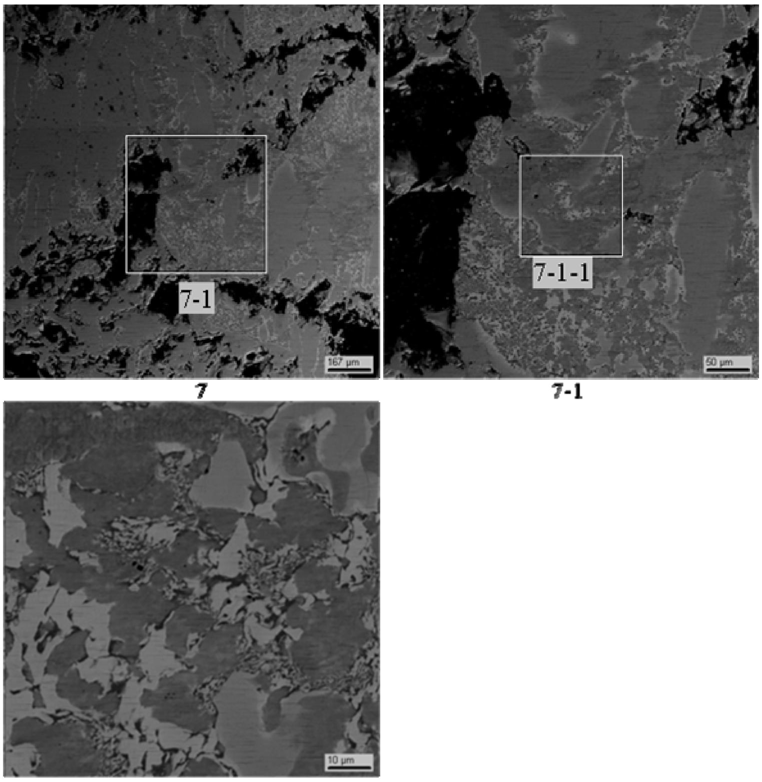

7 7-1

7-1-1

Fig. 3.17 – Microphotographs of Region 7

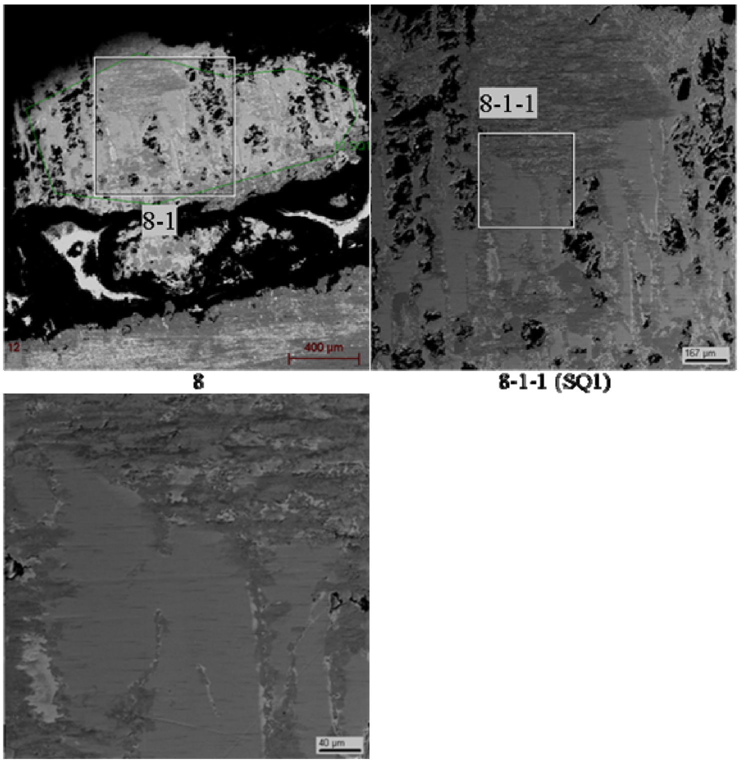

8 8-1-1 (SQ1)

8-1-1

Fig. 3.18 – Microphotographs of Region 8

Table 3.8 – EDX data of Region 8

№		U	Zr	Fe	Cr	Ni	Phase
SQ1	mass%	27.2	16.1	46.2	6.6	3.9	Crystallized melt
	mol.%	8.7	13.5	63.1	9.7	5.0	

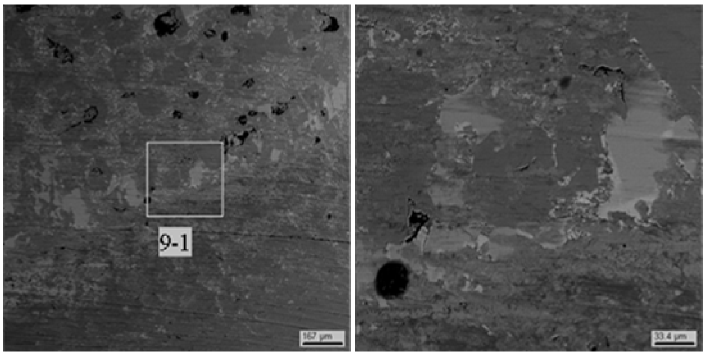

9 9-1

Fig. 3.19 – Microphotographs of Region 9

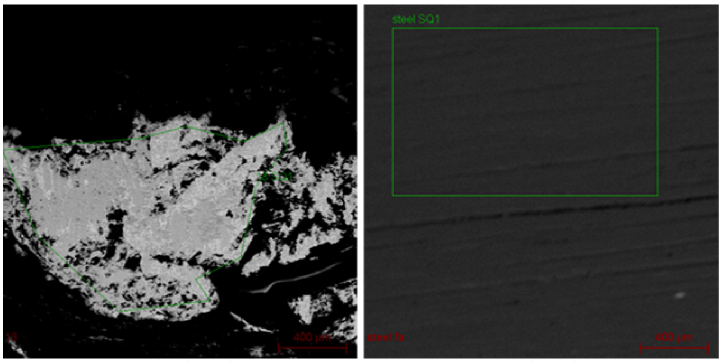

10 (SQ1) 11 (SQ2)

Fig. 3.20 – Microphotographs of regions 10-11

Table 3.9 —EDX data of regions 10-11

№		U	Zr	Fe	Cr	Ni	Si	Phase
SQ1	mass%	24.4	20.8	43.1	7.1	4.7	–	Crystallized melt
	mol.%	7.8	17.3	58.5	10.4	6.0	–	
SQ2	mass%	2.7	0.4	92.4	2.7	1.5	0.3	steel
	mol.%	0.7	0.3	94.1	3.0	1.4	0.6	

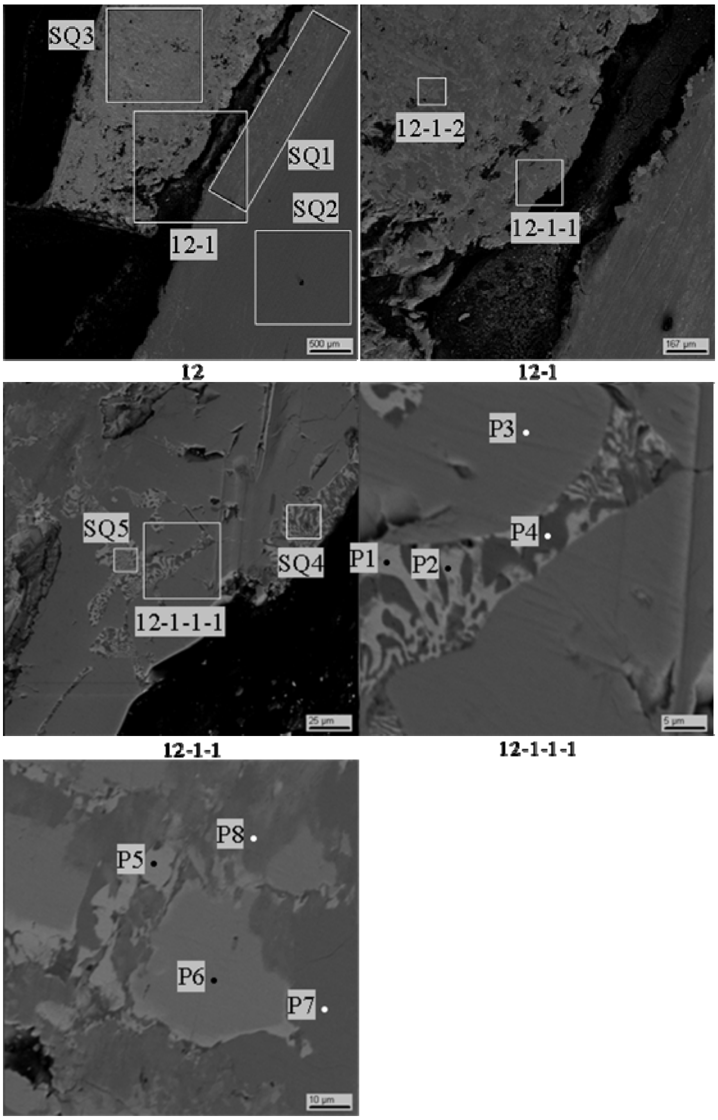

12 12-1

12-1-1 12-1-1-1

12-1-2

Fig. 3.21 – Microphotographs of Region 12

Table 3.10 – EDX data of Region 12

№		U	Zr	Fe	Cr	Ni	Si	Phase
SQ1	mass%	13.5	6.6	62.2	15.5	2.0	0.2	–
	mol.%	3.6	4.6	70.3	18.8	2.2	0.5	
SQ2	mass%	3.6	1.1	90.4	3.2	1.5	0.3	–
	mol.%	0.9	0.7	92.8	3.5	1.5	0.7	
SQ3	mass%	28.8	12.5	47.4	6.7	4.4	0.2	–
	mol.%	9.2	10.4	64.4	9.8	5.7	0.6	
SQ4	mass%	34.1	3.2	50.5	8.9	3.2	–	–

	mol.%	11.0	2.7	69.0	13.1	4.2	–	
SQ5	mass%	31.8	2.4	53.2	9.2	3.5	–	–
	mol.%	9.9	1.9	70.7	13.1	4.4	–	
P1	mass%	46.8	4.3	39.7	3.1	6.2	–	UFe_3
	mol.%	17.6	4.2	63.5	5.4	9.4	–	
P2	mass%	57.6	3.4	32.0	1.6	5.4	–	
	mol.%	24.8	3.8	58.7	3.2	9.4	–	
P3	mass%	10.1	26.8	52.8	6.6	3.2	0.5	$ZrFe_3$
	mol.%	2.9	19.8	63.8	8.6	3.7	1.2	
P4	mass%	10.8	0.7	71.3	15.0	2.2	–	Fe-Cr (azeotropy)
	mol.%	2.7	0.5	77.1	17.4	2.2	–	
P5	mass%	56.8	4.4	31.7	2.2	4.9	–	UFe_3
	mol.%	24.3	4.9	57.9	4.4	8.5	–	
P6	mass%	34.7	15.0	42.0	3.3	4.7	0.2	$(U,Zr)Fe_3$
	mol.%	12.0	13.6	62.0	5.3	6.6	0.6	
P7	mass%	19.9	11.4	55.6	9.2	3.7	0.2	Mixture of phases
	mol.%	5.8	8.6	68.6	12.1	4.4	0.5	
P8	mass%	20.4	8.8	58.6	7.1	4.8	0.3	
	mol.%	5.9	6.6	71.9	9.4	5.6	0.8	

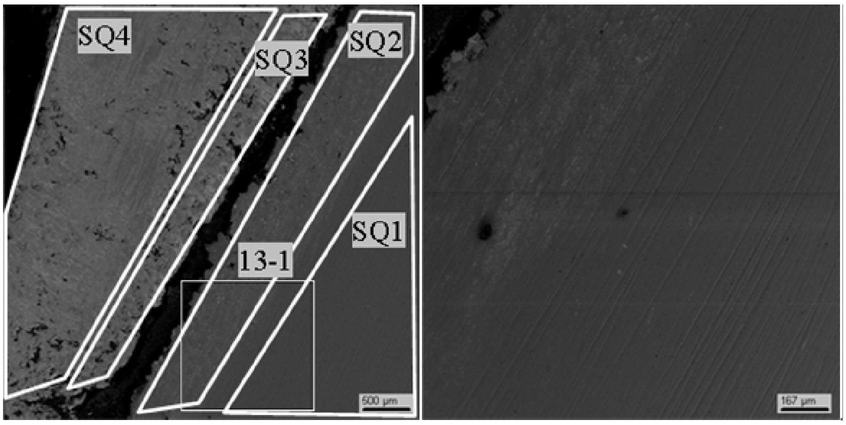

13 13-1

Fig. 3.22 – Microphotographs of Region 13

Table 3.11 – EDX data of Region 13

№		**U**	**Zr**	**Fe**	**Cr**	**Ni**	**Si**	**Phase**
SQ1	mass%	4.6	1.1	89.1	3.2	1.7	0.3	–
	mol.%	1.1	0.7	92.3	3.6	1.6	0.7	
SQ2	mass%	13.1	4.4	64.0	16.0	2.2	0.4	–
	mol.%	3.4	3.0	71.3	19.1	2.3	0.8	
SQ3	mass%	28.3	12.9	48.1	6.9	3.6	0.3	–
	mol.%	9.0	10.6	64.9	9.9	4.7	0.9	
SQ4	mass%	31.5	12.1	44.7	7.4	3.9	0.3	–
	mol.%	10.3	10.3	62.2	11.1	5.2	0.9	

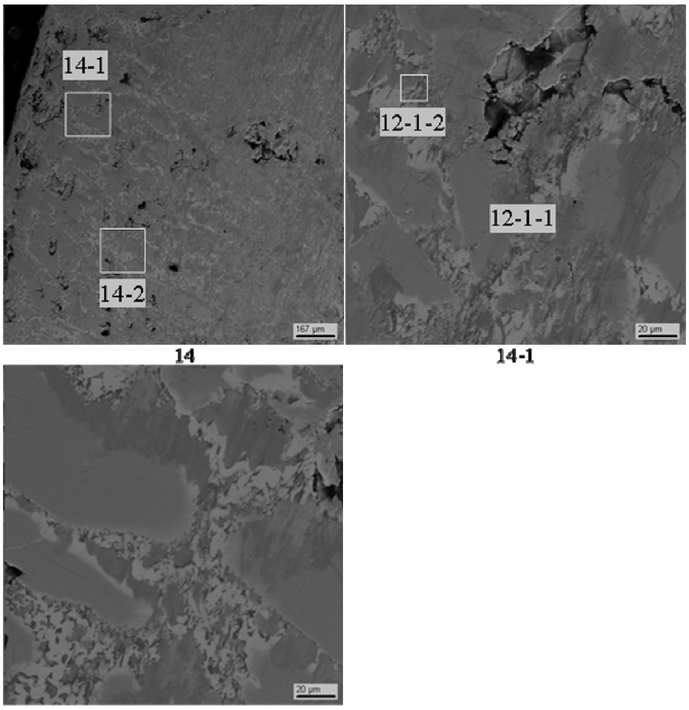

14 14-1

14-2

Fig. 3.23 – Microphotographs of Region 14

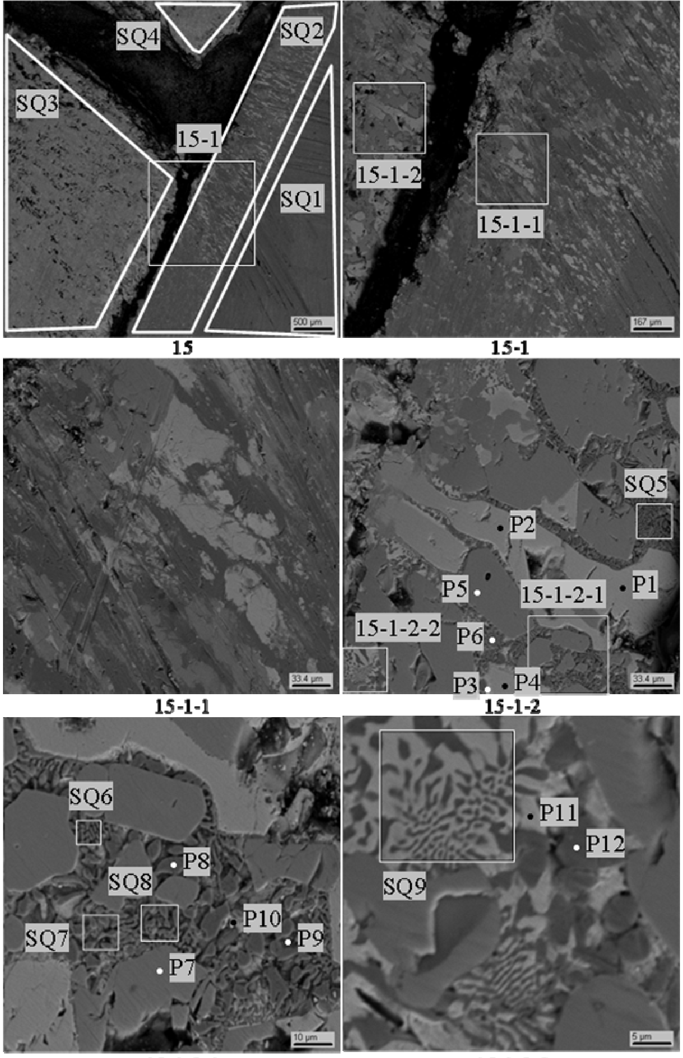

15 15-1

15-1-1 15-1-2

15-1-2-1 15-1-2-2

Fig. 3.24 – Microphotographs of Region 15

Table 3.12 – EDX data of Region 15

№		U	Zr	Fe	Cr	Ni	Si	Phase
SQ1	mass%	4.3	0.9	89.1	3.5	1.9	0.3	–
	mol.%	1.1	0.6	92.1	3.9	1.8	0.6	
SQ2	mass%	19.3	6.8	58.5	12.2	2.7	0.5	–
	mol.%	5.4	5.0	69.8	15.7	3.1	1.1	
SQ3	mass%	27.1	12.2	49.2	7.3	3.9	0.3	–
	mol.%	8.5	9.9	65.4	10.4	5.0	0.8	
SQ4	mass%	29.0	11.6	47.8	7.3	3.9	0.4	–
	mol.%	9.2	9.6	64.5	10.6	5.0	1.1	
SQ5	mass%	14.7	8.8	60.0	13.8	2.5	0.2	“Dark” eutectics with Zr
	mol.%	4.0	6.3	69.4	17.2	2.7	0.5	
SQ6	mass%	14.0	1.1	64.5	17.9	2.4	0.1	“Dark” eutectics
	mol.%	3.6	0.8	71.6	21.3	2.5	0.2	
SQ7	mass%	18.0	2.1	61.7	15.6	2.7	–	
	mol.%	4.9	1.5	71.4	19.4	2.9	–	
SQ8	mass%	11.4	0.7	66.6	19.1	2.2	–	
	mol.%	2.9	0.5	72.1	22.3	2.2	–	
SQ9	mass%	30.9	3.9	50.9	10.3	4.0	0.1	«Light» eutectics
	mol.%	9.6	3.1	67.3	14.7	5.0	0.3	
P1	mass%	35.7	12.8	42.5	3.8	4.9	0.2	$(U,Zr)Fe_3$
	mol.%	12.3	11.6	62.5	6.1	6.9	0.6	
P2	mass%	34.6	16.1	41.0	3.6	4.3	0.3	
	mol.%	12.0	14.6	60.7	5.8	6.1	0.9	
P3	mass%	37.2	14.8	40.2	3.4	4.2	0.2	
	mol.%	13.2	13.7	60.8	5.6	6.1	0.6	
P4	mass%	36.3	14.9	40.3	3.9	4.3	0.2	
	mol.%	12.8	13.7	60.4	6.3	6.2	0.6	
P5	mass%	8.2	27.0	53.9	7.1	3.3	0.5	$ZrFe_3$
	mol.%	2.3	19.6	64.1	9.1	3.7	1.2	
P6	mass%	15.1	27.5	44.6	10.9	1.9	–	Mixture of phases
	mol.%	4.5	21.4	56.8	15.0	2.3	–	
P7	mass%	10.7	23.8	54.1	7.7	3.4	0.3	$ZrFe_3$
	mol.%	3.0	17.5	64.9	10.0	3.9	0.7	
P8	mass%	1.8	0.2	76.4	19.6	1.9	–	Fe-Cr (azeotropy)
	mol.%	0.4	0.1	76.5	21.1	1.8	–	
P9	mass%	21.0	4.8	57.7	12.4	4.0	0.2	Mixture of phases
	mol.%	5.9	3.5	69.5	16.0	4.5	0.5	
P10	mass%	27.9	1.9	54.3	11.2	4.6	0.2	
	mol.%	8.3	1.5	68.9	15.3	5.5	0.5	
P11	mass%	56.7	3.7	30.9	1.9	6.7	0.1	$U(Fe,Ni)_3$
	mol.%	24.2	4.1	56.1	3.8	11.6	0.4	
P12	mass%	6.2	0.3	72.8	18.6	2.1	0.1	Fe-Cr (azeotropy)
	mol.%	1.5	0.2	75.4	20.6	2.1	0.2	

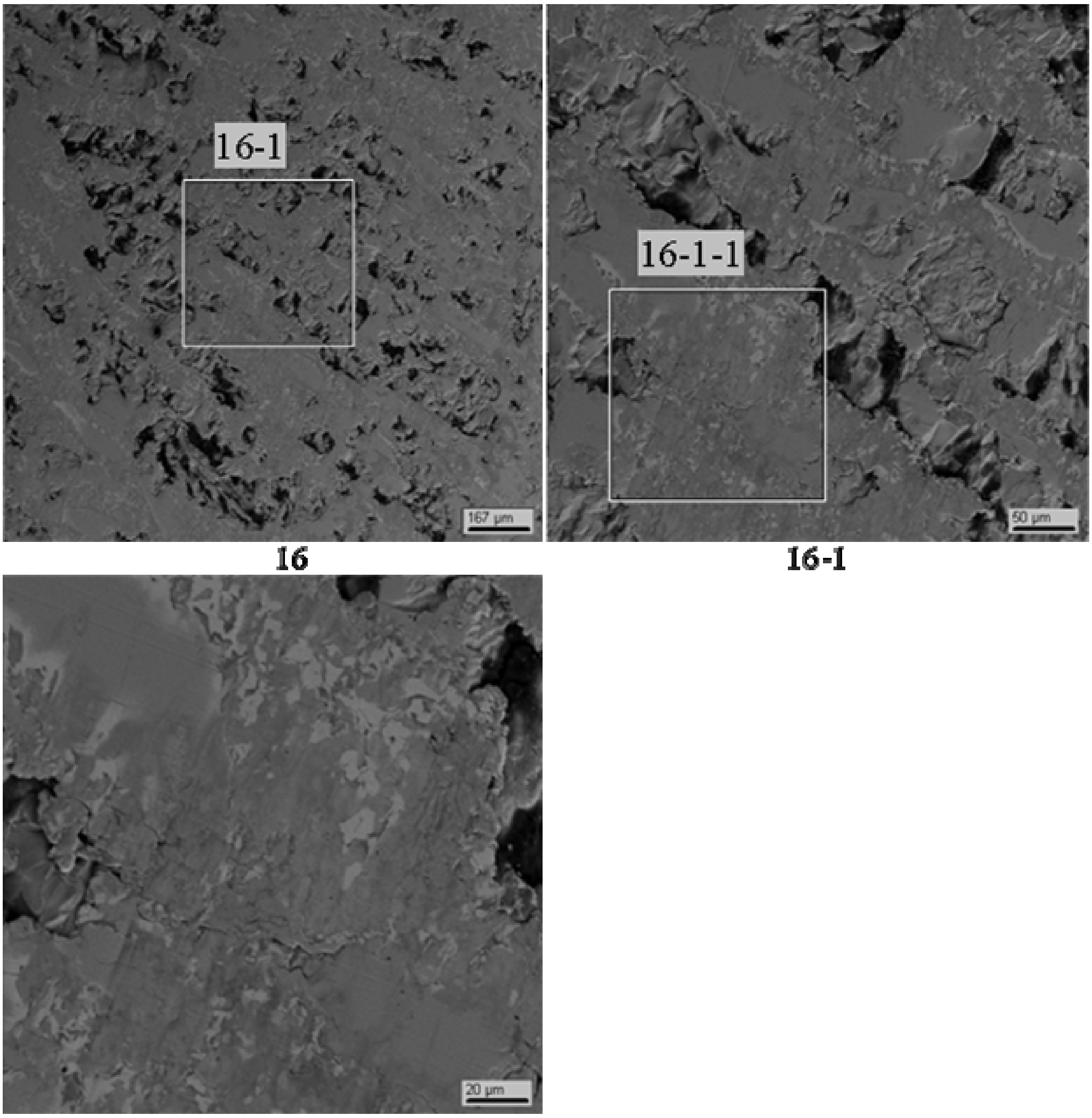

16

16-1

16-1-1

Fig. 3.25 – Microphotographs of Region 16

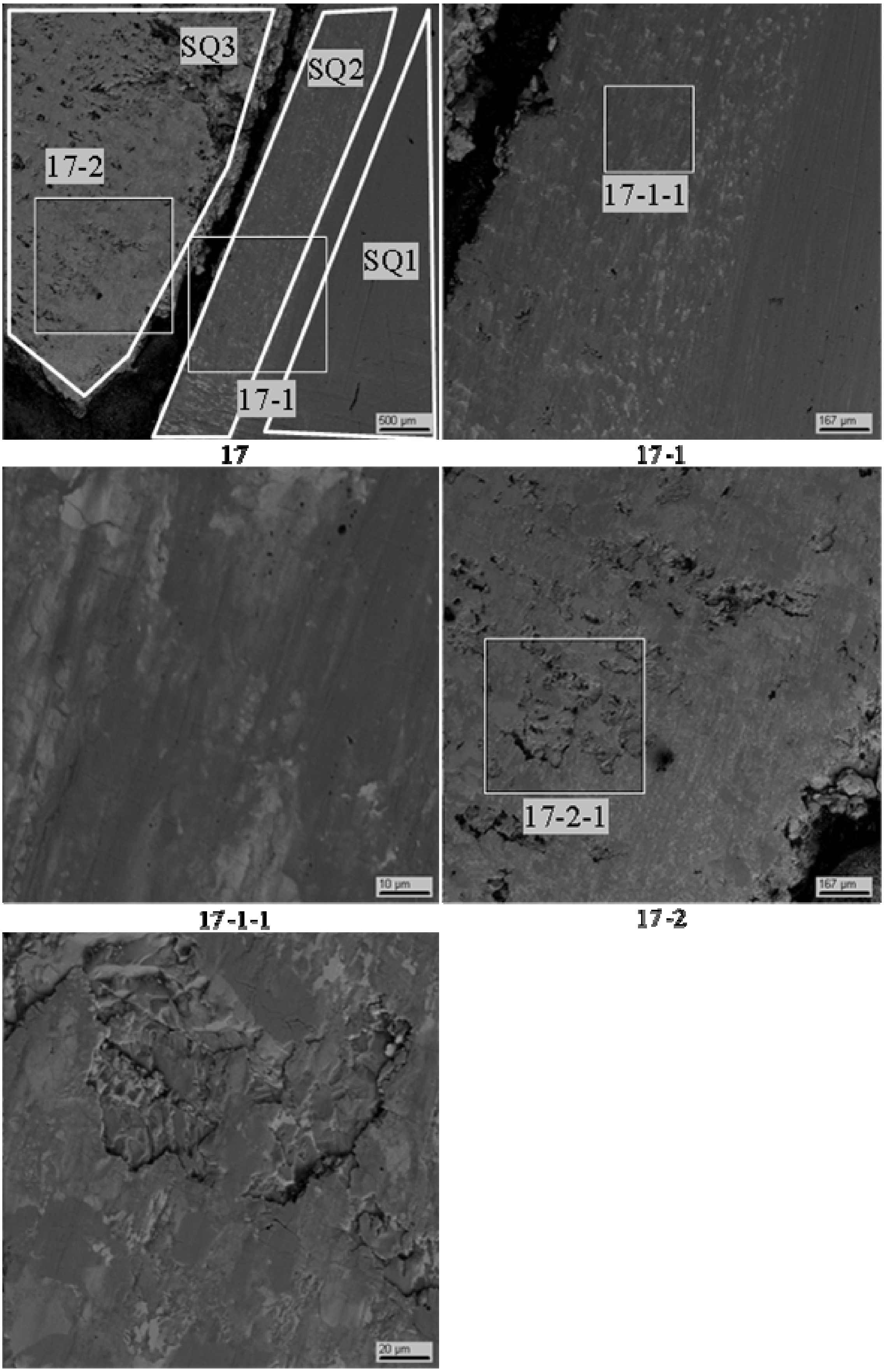

17 **17-1**

17-1-1 **17-2**

17-2-1

Fig. 3.26 – Microphotographs of Region 17

Table 3.13 – EDX data of Region 17

№		U	Zr	Fe	Cr	Ni	Si	Phase
SQ1	mass%	4.5	1.6	87.3	4.3	1.7	0.5	–
	mol.%	1.1	1.0	90.3	4.8	1.7	1.1	
SQ2	mass%	14.7	5.6	61.9	14.8	2.3	0.7	–
	mol.%	3.9	3.9	70.1	18.1	2.5	1.6	
SQ3	mass%	25.4	13.9	48.9	6.7	4.5	0.6	–
	mol.%	7.8	11.2	64.2	9.5	5.6	1.7	

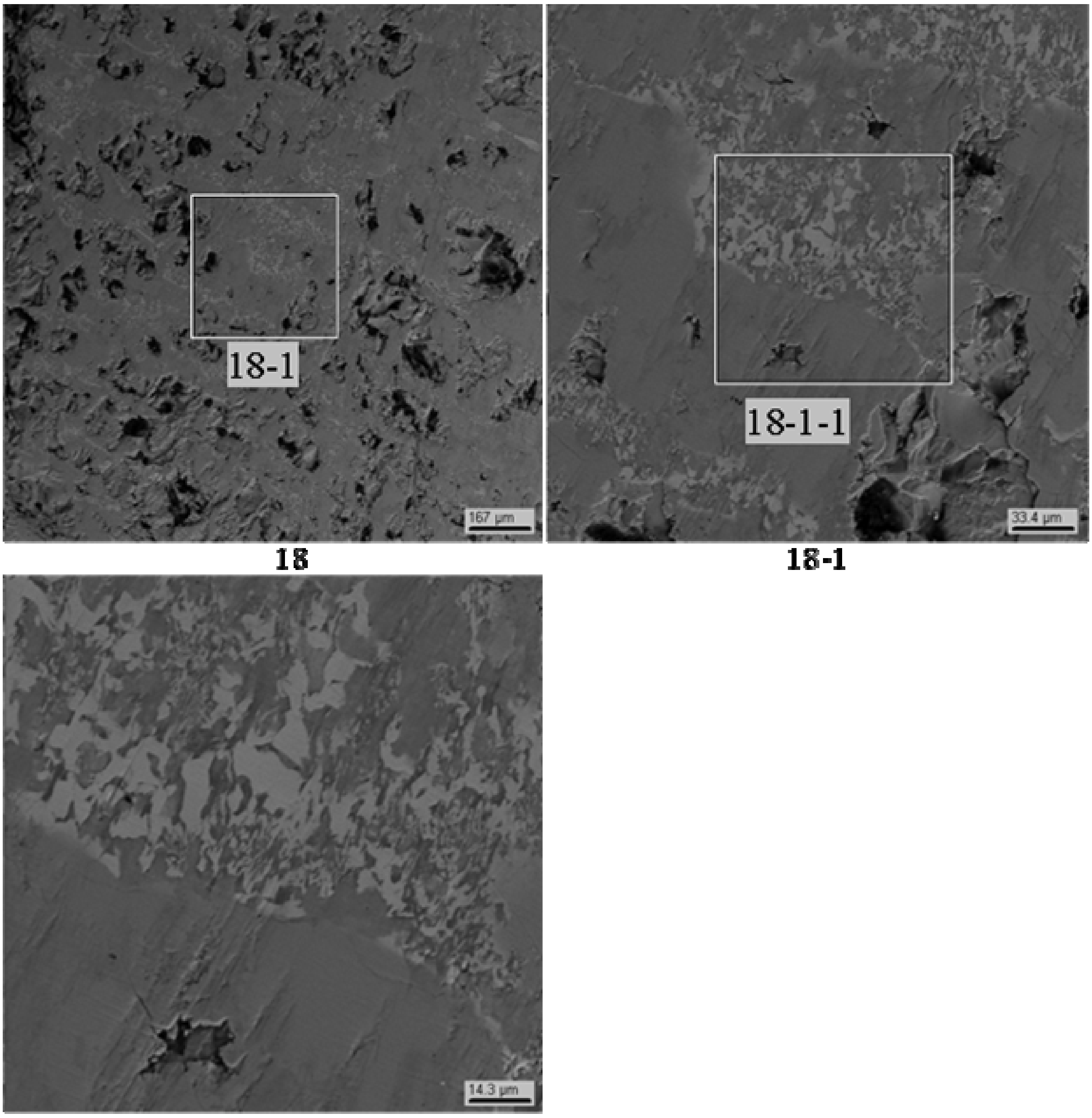

18

18-1

18-1-1

Fig. 3.27 – Microphotographs of Region 18

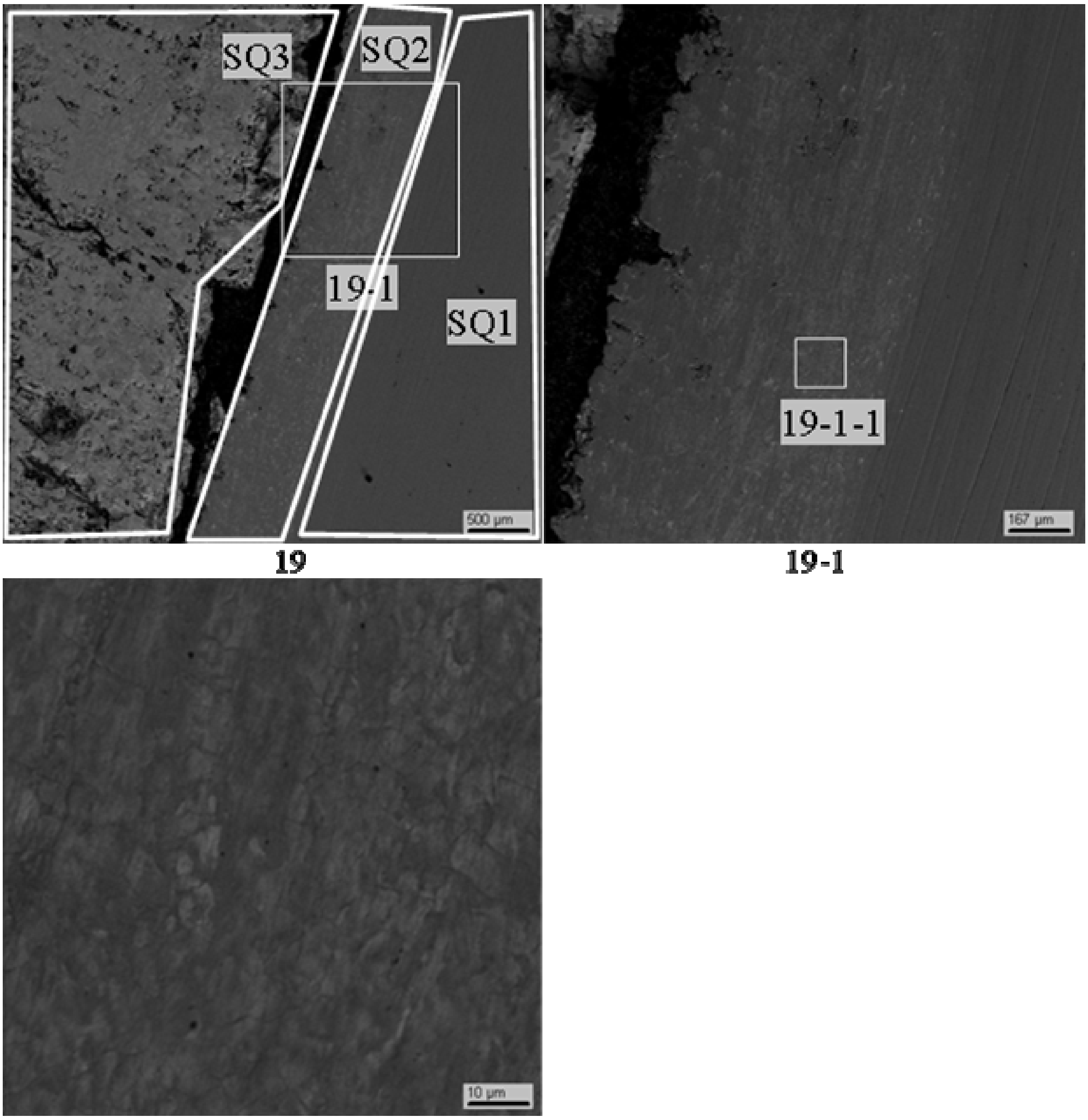

19 **19-1**

19-1-1

Fig. 3.28 – Microphotographs of Region 19

Table 3.14 – EDX data of Region 19

№		U	Zr	Fe	Cr	Ni	Si	Phase
SQ1	mass%	4.5	1.4	88.8	3.3	1.5	0.6	–
	mol.%	1.1	0.9	91.7	3.7	1.5	1.2	
SQ2	mass%	16.1	6.1	61.8	13.4	2.1	0.5	–
	mol.%	4.3	4.3	71.2	16.6	2.3	1.2	
SQ3	mass%	28.7	14.2	46.2	6.8	3.6	0.4	–
	mol.%	9.2	11.9	63.1	10.0	4.7	1.2	

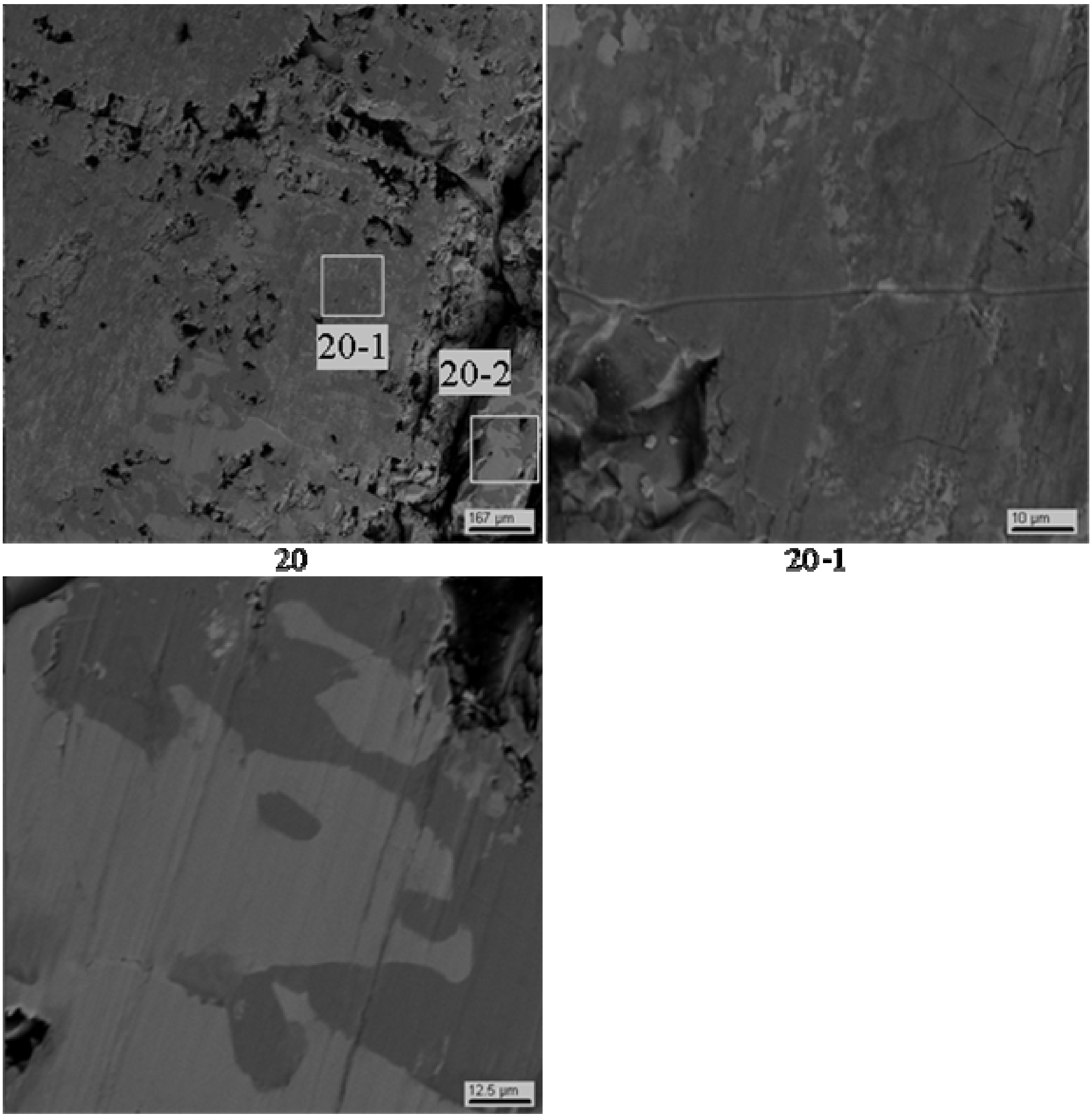

20 20-1

20-2

Fig. 3.29 – Microphotographs of Region 20

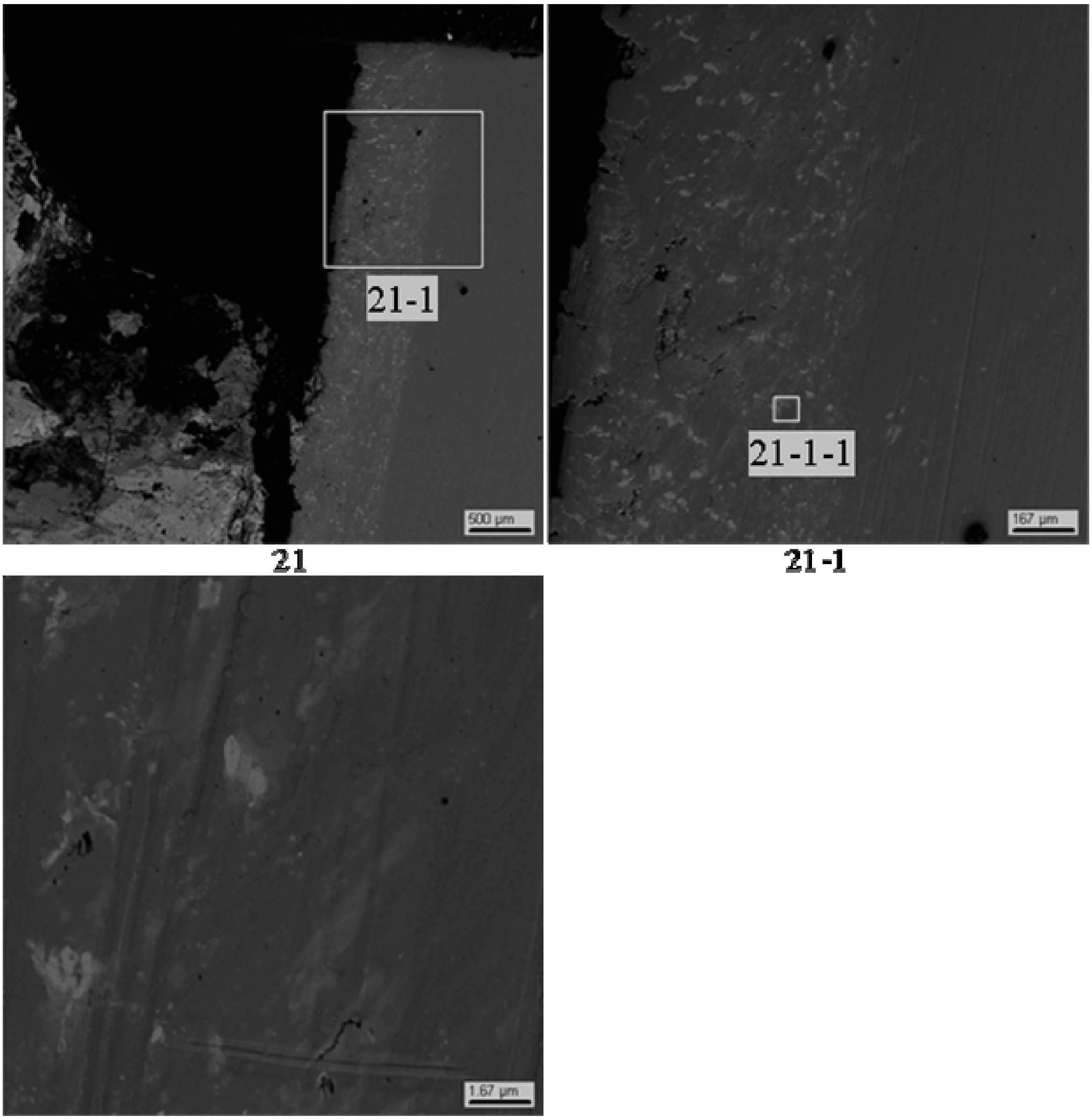

21 21-1

21-1-1

Fig. 3.30 – Microphotographs of Region 21

Fig.. 3.31 shows the schematics of characteristic layers observed on the polished section surface, numbered from steel in the direction of crystallized melt. Table 3.15 gives the statistical processing of the analytical data on the considered zones.

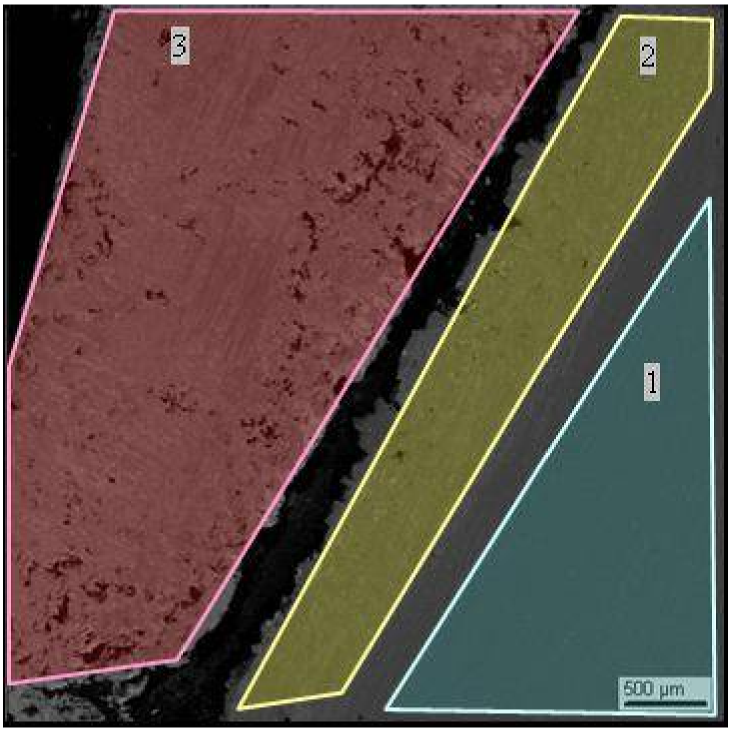

Fig. 3.31 –Schematics of the MCP-8 characteristic zones

Table 3.15 –EDX analysis of MCP-8 characteristic zones

№		U	Zr	Fe	Cr	Ni	Si	Comments
1	mass%	3.9±1.0	1.2±0.6	89.9±4.6	3.2±0.4	1.5±0.2	0.3±0.2	Steel with U, Zr (9 fields) penetrated by diffusion
	mol.%	0.9±0.3	0.8±0.4	92.6±1.4	3.6±0.5	1.5±0.2	0.6±0.4	
2	mass%	16.9±3.7	7.5±2.4	60.4±3.2	12.5±1.8	2.4±0.4	0.2±0.2	Crystallized mushy zone (8 fields)
	mol.%	4.6±1.1	5.3±1.9	70.9±1.1	15.8±2.9	2.7±0.5	0.7±0.6	
3	mass%	26.5±1.8	15.6±3.6	47.1±2.4	6.6±0.6	4.0±0.4	0.2±0.2	Crystallized intermediate mushy zone of the surface crust (16 fields)
	mol.%	8.4±0.8	12.9±3.1	63.5±2.4	9.6±1.0	5.1±0.6	0.5±0.5	

The analysis of steel (zone 1, Fig. 3.31) has shown the presence of melt components in it – uranium and zirconium. The analyzed zones show the presence of these components as dot-like inclusions (Fig. 3.22, region 13-1). The melt components probably penetrated by diffusion. But diffusion channels are practically not found up to the boundary with Zone 2.

Along the whole height of Zone 2 the microstructure is the same (compare with Fig. 3.12, region 2-2 and Fig.. 3.26, region 17-1), and its thickness is about 200÷500 µm (Fig. 3.31, zone 2). Table 3.15 gives the statistical processing of the EDX data on the layer composition in the studied polished sections. The main component is Fe, but U and Zr are also present in considerable quantities. The microstructure of the studied layer testifies to the formation and recrystallizastion of intermetallide phases of $(Zr,U)Fe_3$ and $ZrFe_3$ in it.

On the boundary between Zone 2 and Zone 3 a different vertical pattern is observed in the polished sections. In region 1 of the upper polished section the microstructure of crystallized melt looks like faceted crystals based on the $ZrFe_3$ intermetallide in the fine-dispersion mixture of phases corresponding to the eutectic character of crystallization. The composition of analyzed eutectic zones is given in Table 3.16, line 1.

Table 3.16 - EDX analysis of the eutectic crystallization regions. Experiment MCP-8

#		U	Zr	Fe	Cr	Ni	Comments
1	mass%	30.6±1.5	10.4±4.1	47.8±4.6	7.3±0.7	4.0±0.5	“Light” eutectics, top polished section (5 fields)
	mol.%	9.9±0.4	8.8±3.9	65.5±3.5	10.6±0.6	5.3±0.6	
2	mass%	32.3±1.7	3.2±0.8	51.5±1.2	9.5±0.8	3.6±0.4	“Light” eutectics, bottom polished section (3fields)
	mol.%	10.1±0.7	2.6±0.6	69.0±1.7	13.6±0.8	4.5±0.4	
3	mass%	14.5±3.3	1.3±0.7	64.3±2.3	17.6±1.7	2.4±0.3	“Dark” eutectics, bottom polished section (3 fields)
	mol.%	3.8±1.0	0.9±0.5	71.7±0.4	21.0±1.4	2.6±0.3	

In the bottom part of the lower polished section there are fewer zones of eutectic crystallization. Two types of eutectics are found. Their compositions are given in Table 3.16, lines 2, 3. The main part of the polished section is occupied by the crystals of intermetallide phase of (Zr,U)Fe_3 and $ZrFe_3$.

The analysis of the microstructure changes from the top to bottom zones and the shape of crystals bring a conclusion that the crystals were present in the melt at the moment of heating disconnection, i.e. the layer of crystallized melt adjacent to steel and having a few-mm thickness was mushy at the time. After the temperature limit of steel dissolution on the boundary of zones 2 and 1 was reached, the eutectic mechanism of interaction was replaced by diffusion (Fig.. 3.31).

4. DISCUSSION OF RESULTS

Before the discussion of MCP-8 data it is necessary to remind that in all experiments on the interaction between the VVER steel and melt in the neutral atmosphere (MC6÷MC9, MCP-1) steel corrosion was caused by its dissolution (eutectic melting) in the metallic melt of the interaction zone (IZ) having a negligibly small content of oxygen [12]. In a general case the IZ is mushy. The IZ was formed after the start of interaction between specimens and suboxidized corium melt. In MC9 the metallic melt of the two-liquid pool was the first to interact, but in the course of interaction it was not only total Fe initially introduced into the melt, but also a part of Fe partitioned into the IZ from the specimen, which evaporated from the high-temperature molten pool [1].

So in all previous tests the steel specimen interacted with the oxidic-metallic system, but directly – with its metallic part (with IZ). In our opinion the spatial orientation of the interaction interface has an insignificant influence on the steel corrosion, because it is mostly determined by the physicochemical processes. In the experimental conditions they are hardly influenced by the gravitation. Differences in the microstructure and composition of the zones from upper and lower templates (Table 3.16) are not principal, but we should keep in mind a small height of the specimen, in real conditions it is much larger.

For the MCP-8 analysis we should prove that the oxygen content in its metallic melt is small, as well as in all previous experiments. In MCP-8 the initial charge composition contained U and Zr oxides in large quantities in all parts of the metallic charge except the gap with the specimen. If the temperature of metallic melt was quite high in the experiment, it could dissolve a certain amount of oxygen.

To evaluate the MCP-8 melt temperature, the integrated calculations of the electromagnetic and hydrodynamic pool models were made. On the boundary with the specimen the liquidus temperature for the metallic charge composition (≈1220ºC) was assumed. For other surfaces the presence of oxidic crust was assumed. The results of calculations are given in Fig. 4.1.

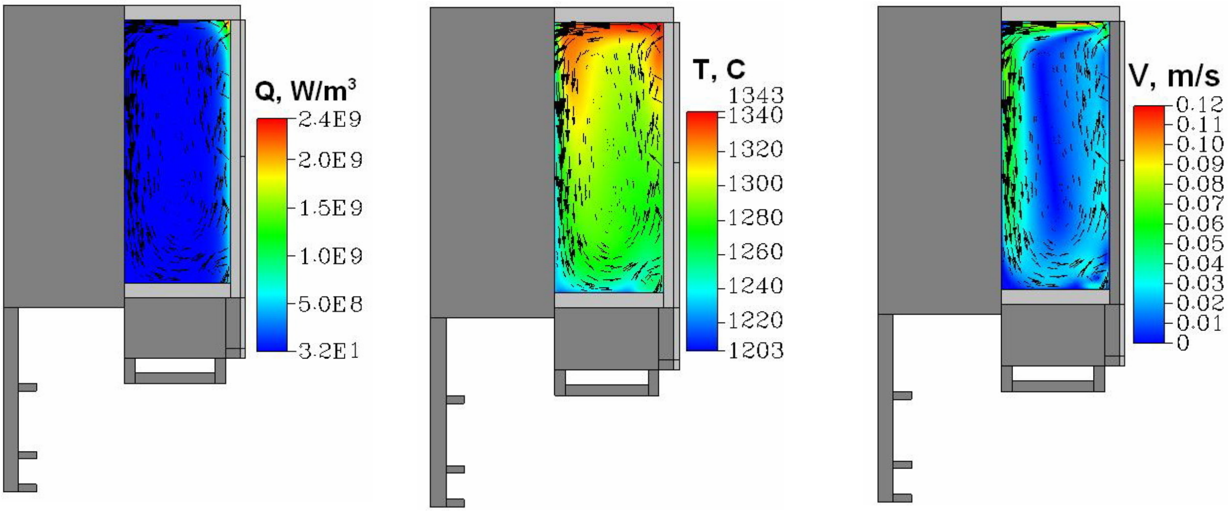

Fig. 4.1 – Distribution of heat, temperature and speed in the molten pool

It follows from the figure that the melt average temperature is ≈1280ºC. At such low temperature the oxygen solubility is extremely small and, consequently, an assumption that in MCP-8, as well as in other experiments, the specimen interacted with metallic melt, is true.

Now let us address the MCP-8 results and, first of all, causes for the temperature on the final boundary of the steel specimen corrosion. Note that in accordance with the calculated specimen temperature conditions it was 1050÷1150°C.

The MC6÷MC9, MCP-1 analysis considered the sections of U-Zr-Fe phase diagram at the U/Zr ratios in the system corresponding to the experimental U/Zr values in the IZ [13]. They are shown in Fig. 4.2. The experimental temperature values on the final boundary of specimen corrosion and corresponding mass fractions of steel in the IZ are shown as dots with error bars.

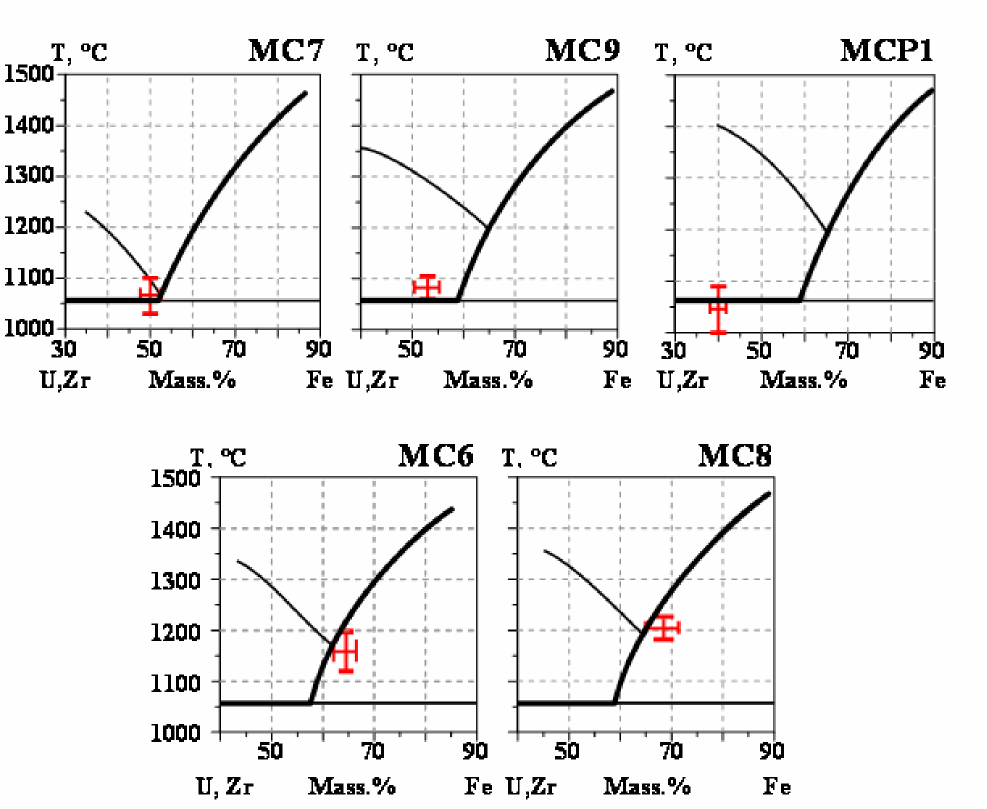

Fig. 4.2 – The U-Zr-Fe phase diagram sections

The analysis was used to propose a qualitative model of corrosion process [13], in accordance with which the final temperature boundary of corrosion (temperature limit of steel dissolution in the IZ) is the solidus temperature, if the IZ composition is in the domain of the U, Zr primary crystallization, or liquidus temperature, if the IZ composition is in the domain of Fe primary crystallization.

Let us consider if MCP-8 data correspond to the mentioned model. Fig. 4.3 shows the phase diagram section of the (U,Zr,Cr,Ni)-Fe system (calculated with GEMINI2/NUCLEA) with the U-Zr-Cr-Ni ratio determined by the ingot XRF. The figure with horizontal dashed lines shows the range, in which temperature on the final specimen corrosion boundary was determined, and vertical dashed line – ingot composition (composition of metallic melt by the time of corrosion finish).

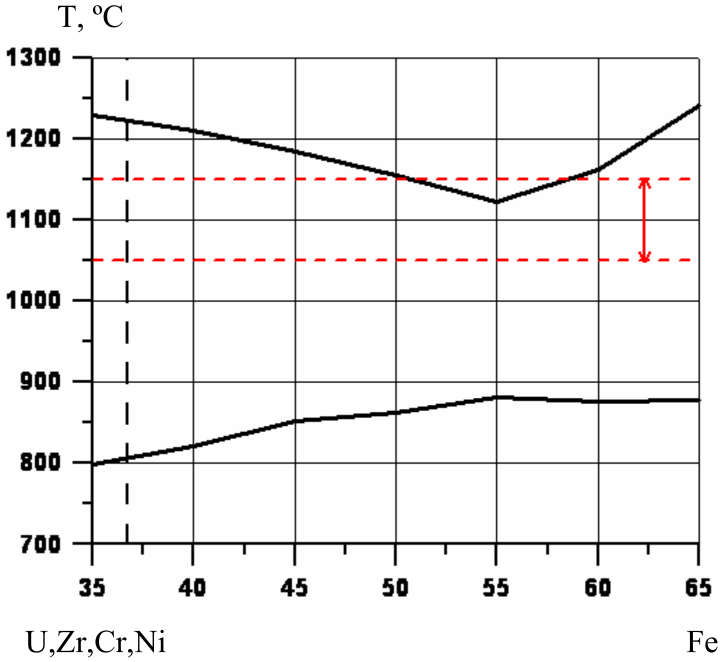

Fig. 4.3 – Sections of the (U,Zr,Cr,Ni)-Fe phase diagram

It can be seen from the figure that in MCP-8 the temperature of final corrosion boundary (within the accepted accuracy) is close to the minimum temperature on the liquidus line (≈1100ºC) and it is considerably higher than the temperature on the solidus line. It does not agree with the model discussed above, in accordance with which for the melt composition in the primary crystallization zone of U,Zr,Cr,Ni (not Fe), i.e. for the MCP-8 conditions, the temperature of the final corrosion boundary must be on the solidus line. Then the value of this temperature would be 800÷900°C.

To explain this controversy let us first consider the processes, which determinate steel corrosion in the MCP-8 conditions. At the initial stage a solid crust is formed on the specimen surface; it contains the compounds of components from the primary melt crystallization zone in accordance with the phase diagram of Fig. 4.3. On the surface of the interface with the melt – liquidus temperature. On the surface of the interface with the specimen (in the part, where temperature exceeds the minimum liquidus temperature, see the diagram of Fig. 4.3) the steel dissolution (eutectic melting) takes place. The composition of the formed liquid phase is close to the composition corresponding to the minimum liquidus temperature. As the corrosion depth increases, the thickness of surface crust impregnation by the liquid phase grows. Corrosion stops after the minimum liquidus temperature is reached on the interface surface, because the increase of Fe content in the layer adjacent to the interface at this minimum temperature transfers it to the domain of Fe primary crystallization, i.e. makes further dissolution impossible.

The SEM/EDX data confirm the discussed model of corrosion. In accordance with the data of Table 3.15 and Fig. 3.31 the Fe content on the boundary with the specimen is ≈60% mass, and it rapidly decreases to ≈47% mass at 1÷2 mm from the boundary. In accordance with XRF at a larger distance from the boundary the Fe content was ≈37% mass, which is likely to be close to the melt average composition. It can be seen from Fig. 4.3 that the Fe content of 60% mass is close to the composition corresponding to the minimum liquidus temperature.

It should be noted that the GEMINI2/NUCLEA verification for the U-Zr-Cr-Ni-Fe-O compositions near the miscibility gap is in progress. Therefore, the accuracy of completed thermodynamic modeling is not evident. So the phase diagram section in Fig. 4.3 is rather conventional, though we believe that in the first approximation it can be applied for the current, basically qualitative, analysis.

The remaining unclear point is the reason, for which the steel corrosion stop temperature in MC7, MC9 and MCP-1 is different from MCP-8.

As an example for comparison let us consider the SEM/EDX data of the MCP-1 IZ. Fig. 4.2 shows the phase diagram section for these experimental conditions. The IZ composition is in the U, Zr primary crystallization domain. Temperature on the final corrosion boundary was ≈1050°C, it corresponds to the solidus temperature, and minimum temperature on the liquidus line – ≈1200°C. Fig. 4.4 shows SEM-images of the IZ – steel specimen interaction interface and determined EDX composition of the IZ close to the boundary with steel. The Fe content close to the MCP-1 interaction interface 51.2% mass (Fig. 4.4). It is evident that when the interaction front had 1200°C, the Fe content was not larger than this value, which corresponds to the primary crystallization domain from the U, Zr side (Fig. 4.2). For that reason in MCP-1 corrosion continued until the solidus temperature isotherm was reached. Unfortunately in MC7 and MC9 the results of such analysis are less representative.

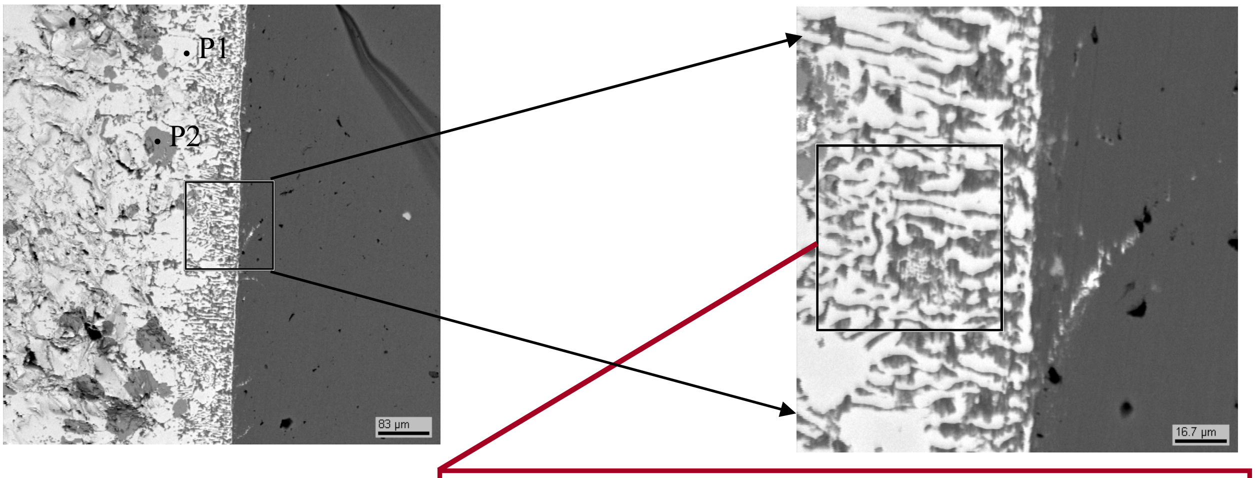

U – 38.3; Zr – 6.9; Fe – 51.2; Cr – 1.9; Ni – 0.8, mass %

Fig. 4.4 – SEM/EDX MCP-1

The results of SEM/EDX analysis explain different temperatures of the final corrosion boundary in MCP-8 and MCP-1 by the difference in melt compositions near the interaction interface. In both cases they are different from the average melt compositions in the direction of higher Fe content, but only in MCP-8 the content of Fe grows to such a high value, at which the corrosion stops when the front reaches the liquidus temperature, not solidus, as in other experiments. But the difference in the Fe content near the interaction interface is not clear, It can be assumed that it is related to the principal difference of MCP-8 – only in this experiment the one-liquid metallic system interacted with the specimen (in others – the two-liquid one). The repartitioning between the IZ and oxidic liquid probably reduces the non-uniformity of Fe content in the IZ and, consequently, its content near the interaction interface.

Now let us consider the corrosion kinetics. From Fig. 2.8 it is evident that "fast" corrosion started at 8800 s. Taking into account that the predetermined specimen temperature condition was established approx. at. 7200 s (Fig. 2.6) the duration of incubation period is ≈1600 s. This value is considerably higher than in MC9 (≈200 s), in which at the initial stage of the test, like in MCP-8, the metallic melt was interacting with the specimen, but much less than in all other experiments on the specimen interaction with the suboxidized corium melt (8000…16000 s).

The data on corrosion kinetics provided by MC6…MC9 experiments were previously summarized by correlation (4.1) [14].

$$\frac{dh}{dt} = 0.46 \cdot 10^{-4} \sqrt{T_{int} - T_B}, \quad mm/s \tag{4.1}$$

Using the same structure of correlation as (4.1), the correlation (4.2) was produced for the MCP-8 data, which is different from (4.1) only by the value of the fixed factor, which is approximately 15% less than in (4.1).

$$\frac{dh}{dt} = 0.39 \cdot 10^{-4} \sqrt{T_{int} - T_B}, \quad mm/s \tag{4.2}$$

The “fast” corrosion kinetics is shown in Fig. 4.5. The lower horizontal axis – time from the corrosion start, the upper – from the MCP-8 beginning.

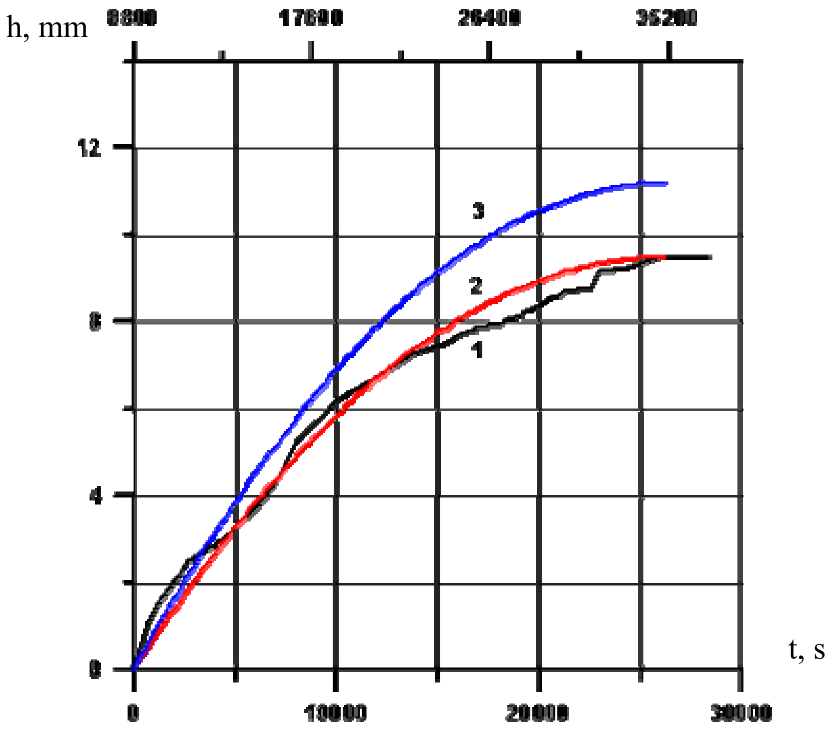

1 – MCP-8 online measurements; 2 – correlation (4.2); 3 – correlation (4.1)
Fig. 4.5 – Corrosion kinetics

Conclusions

- The experiment has determined kinetics, final depth and saturation temperature of the VVER steel corrosion at its interaction with molten corium having mass%: 39U + 14Zr + 48SS at the vertical position of the interaction interface, initial temperature on the surface ~1400ºC and heat flux from melt to steel ~1 MW/m^2.
- Temperature, at which the steel corrosion stopped in the MCP-8 conditions is ≈1100°C, it approximately corresponds to the minimum temperature on the liquidus line in the section of the phase diagram of the (U,Zr,Cr,Ni)-Fe system determined by the GEMINI/NUCLEA code. The MCP-8 IZ composition has a qualitative similarity to that of MC7, MC9, MCP-1 (in terms of its difference from the minimum liquidus temperature composition), the solidus temperature being the corrosion temperature limit. So a probable explanation to the difference in results is that the MCP-8 steel interacted with the one-liquid metallic system, and specimens in all other above-mentioned tests – with metallic liquid of the two-liquid system.
- The correlation describing «fast” steel corrosion in MCP-8 is close to a similar correlation produced in the summary of the MC6…MC9 data.

REFERENCES

1. Investigation of corium melt interaction with NPP reactor vessel steel (METCOR). ISTC Project № 833.2-2003. Final Technical Report (2006).
2. Investigation of the interaction between the corium melt and vessel steel in the neutral above-melt atmosphere at the vertical position of the interaction interface. Experiment MCP-1. ISTC Project 3592 (METCOR-P). Intermediate report. 2007. (In Russian).
3. N.F. Losev. Qualitative X-ray fluorescence analysis. M. Nauka, 1969. (In Russian).
4. D. Skug, D. West. The basics of analytical chemistry. V.1,2. M.: Mir, 1979. (In Russian).
5. V.G. Goriushina, E.V. Romanova, T.A. Archakova, Colorimetry methods for Zr evaluation in alloys // Industrial laboratory, 1961, V. 27, №7, s. 795-797. (In Russian).
6. S.V. Elinson, T.I. Nezhnova, Photometric evaluation of Zr in niobium and other metals // Industrial laboratory, 1964. T. 30, №4, s. 396-399. (In Russian).
7. E. Sendel. Colorimetry methods for determining traces of metal. M.: Mir, 1964. (In Russian). Лена, подправьте, пожалуйста, ссылки с учетом повтора [12]
8. D.I. Ryabchikov, M.M. Seniavin. Analytical chemistry of uranium. M.: USSR Academy of Sciences . 1962. (In Russian).
9. V.F. Lukianov, S.B. Savin, I.V, Nikolskaya. Photometric determination of U microquantities with reagent arsenazo III. J of ACh., XV, issue.3. 1960. (In Russian).
10. V.K. Markov et al. Uranium. Methods for its evaluation. M.: Atomizdat 1964. (In Russian).
11. GOST 4011-72. Drinking water. Methods for determining the mass concentration of total iron. Regulatory document, M. 1972. (In Russian).
12. S.V. Bechta, V.S. Granovsky, E.V. Krushinov et al. Corium Phase Equilibria based on MASCA, METCOR and CORPHAD Results, Nucl. Eng. Des. 238 (2008), pp. 2761-2771.
13. Interaction of suboxidized corium melt with vessel steel of European reactors. Experiment MCP-5. ISTC Project 3592 (METCOR-P). Intermediate report. 2010. (In Russian).
14. S.V. Bechta, V.B. Khabensky, E.V. Krushinov et al. Experimental Study of Interaction Between Suboxidized Corium and Reactor Vessel Steel, Proc. of ICAPP′06, Reno, USA, June 4-8, 2006. Paper 6054.